

**Controlled Deformation and Raman Lasing in Microdroplets  
Standing on a Superhydrophobic Surface**

**by**

**Saime ıgdem Yorulmaz**

**A Thesis Submitted to the  
Graduate School of Science  
in Partial Fulfillment of the Requirements for  
the Degree of**

**Master of Science  
in  
Physics**

**Koc University  
August 2009**

Koc University  
Graduate School of Sciences and Engineering

This is to certify that I have examined this copy of a master's thesis by

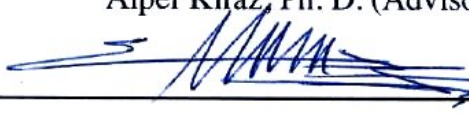
Saime ıgdem Yorulmaz

and have found that it is complete and satisfactory in all respects,  
and that any and all revisions required by the final  
examining committee have been made.

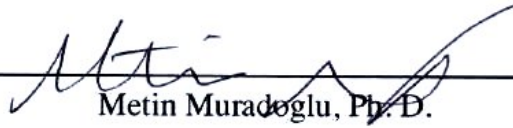
Committee Members:



Alper Kiraz, Ph. D. (Advisor)



B. Erdem Alaca, Ph. D.



Metin Muradođlu, Ph. D.

Date:

10/08/2009

## ABSTRACT

Liquid microdroplets are ideally suited for applications that benefit from the properties of the whispering gallery modes (WGMs) because of their spherical shapes, smooth surfaces, biocompatibility, and flexible nature. In this thesis, we present nondegeneracy in WGMs as a result of deformation in the glycerol-water microdroplets using uniform electric field. Raman lasing from individual pure water microdroplets standing on a superhydrophobic surface is also presented in this thesis.

A liquid microcavity provides relatively easy control of its shape due to its viscous and flexible nature. An applied external force, electric field, or control of the evaporation/condensation kinetics can change the shape of the liquid microdroplets. We demonstrated controlled lifting of the azimuthal degeneracy of the WGMs of glycerol water microdroplets standing on a superhydrophobic surface by using a uniform electric field. A good agreement was observed between the measured spectral positions of the nondegenerate WGMs. Our results revealed fewer azimuthal modes than expected from an ideal spherical microdroplet due to the truncation by the surface. We used this difference to estimate the contact angles of the microdroplets.

Liquid microdroplets are also attractive in developing low threshold Raman lasers due to their high quality factors and small mode volumes. By using pure water microdroplets, we demonstrated Raman lasing near 650 nm. In the experiments, microdroplets were excited by a pulsed, frequency-doubled Nd:YAG laser at 532 nm. Intense laser emission was observed at frequencies corresponding to the WGM resonances of the water microdroplets near 650 nm where Raman resonances due to OH-stretching bonds of water are located. On-off behavior was observed during lasing and the average temporal inter-burst separation was determined from the time-dependent intensity traces.

## ÖZET

Sıvı mikrodamlacıklar, küresel şekli, pürüzsüz yüzeyi, biyo-uyumluluğu ve esnek yapısından dolayı, fısıldayan galeri kiplerinin (FGK) özelliklerinden faydalanan uygulamalarda idealdir. Bu tezde, ilk olarak gliserol-su mikrodamlacıklarının düzgün elektrik alan kullanılarak deforme edilmesi sonucu FGK'lerdeki dejenere olmama durumunu gösteriyoruz. Daha sonra, su tutmayan yüzey üzerinde duran saf su damlacıklarından elde edilen Raman lazer ışımalarını sunuyoruz.

Sıvı bir mikrokovuk, akışkan ve esnek yapısından dolayı göreceli olarak şekilde kolay bir kontrol sağlar. Dışarıdan uygulanan kuvvet, elektrik alan, ya da buharlaşma/yoğunlaşma kinetiği sıvı mikrodamlacıkların şeklini değiştirebilir. Düzgün elektrik alan kullanarak, su tutmayan yüzey üzerindeki gliserol-su mikrodamlacıklarının FGK'lerindeki açısız bozulmayı kontrollü bir şekilde ortaya çıkarıyoruz. Dejenere olmayan FGK'lerin ölçülmüş spektral pozisyonları arasında iyi bir uyum gözlemledik. Deney sonuçlarımıza göre kullandığımız mikrodamlacıklar yüzey tarafından kesildiği için, ideal küresel bir mikrodamlacıktan beklenen açısız kip sayısından daha az açısız kip elde ettik. Bu farkı mikrodamlacıkların su tutmayan yüzey üzerindeki kontak açılarını tahmin etmede kullanıyoruz.

Sıvı mikrodamlacıklar, yüksek kalite faktörleriyle ve küçük kip hacimleriyle düşük eşik değerli Raman lazeri geliştirmek için de kullanılırlar. Saf su mikrodamlacıkları kullanarak, 650 nm civarında Raman lazer ışımalarını gösterdik. Deneylerimizde, mikrodamlacıklar 532 nm'de çalışan iki kat sıklıklı darbeli bir lazer ile uyarıldı. 650 nm'de su damlacıklarının FGK rezonansları, suyun OH-bağlarının gerilmesi sonucu Raman rezonansı ile aynı yerdedir ve bu rezonansa karşılık gelen frekansta yoğun lazer emisyonu görülür. Lazer ışımaları sırasında açık-kapalı davranışı gözlemlendi ve ortalama geçici ışımalar arası ayrılma, zamana bağlı yoğunluk izlemesiyle belirlenir.

## ACKNOWLEDGEMENTS

I would like to express my gratitude to my supervisor, Dr. Alper Kiraz, for his support during my research work. His encouragement and guidance from initial to the final level of my work enabled me to complete my projects successfully.

I would like to thank Dr. Erdem Alaca who supported and guided me during the cleanroom experiments. It was an honor for me to benefit from his deep knowledge. I would also like to thank Dr. Metin Muradoglu for fruitful discussions. Special thanks to Dr. Michael Mestre, it was a pleasure for me to work with him. I would also like to thank him for his friendship.

Thanks also to my friends from Nano-Optics Research Laboratory for their contributions and help during my experiments. Thanks to Mehmet Salih Kılıç for teaching me the usage of cleanroom equipments.

I would like to thank my parents for their understanding, encouragement and patience at all times. I also thank my second mum and dad whose love and support make me feel better.

Above all, I owe my deepest gratitude to my dearest husband, Mustafa Yorulmaz. It is a priceless feeling to have you beside me in the past, present, and future. Thank you so much for your faithful love and endless help. This thesis wouldn't exist without you.

## TABLE OF CONTENTS

|  |             |
|--|-------------|
| <b>List of Tables</b>  | <b>viii</b> |
| <b>List of Figures</b>   | <b>ix</b>   |
| <b>Nomenclature</b>  | <b>xii</b>  |
| <b>Chapter 1: Introduction</b>   | <b>1</b>    |
| 1.1 Overview.....  | 1           |
| 1.2 Thesis Outline.....  | 4           |
| 1.3 Surface Preparation and Microdroplet Generation.....               | 5           |
| <b>Chapter 2: Cavity Modes of Microspheres</b>                         | <b>7</b>    |
| 2.1 Introduction.....  | 7           |
| 2.2 Whispering Gallery Modes (WGMs).....                               | 8           |
| 2.2.1 Ray and Wave Optics.....   | 9           |
| 2.2.2 Mie Theory: Light Scatterig of a Dielectric Sphere.....          | 10          |
| 2.2.3 Quality Factor (Q) in WGMs.....                                  | 13          |
| <b>Chapter 3: Controlled Observation of Nondegenerate Cavity Modes</b> | <b>14</b>   |
| 3.1 Introduction.....  | 14          |
| 3.2 Liquid Droplet Deformation in DC Electric Field.....               | 15          |
| 3.3 Azimuthal Degeneracy inWGMs.....                                   | 16          |
| 3.4 Sample Preparation and Experimental Setup.....                     | 17          |
| 3.4.1 Fabrication Process of Indium Tin Oxide Contacts.....            | 17          |

|   |           |
|---|-----------|
| 3.4.2 Superhydrophobic Coating and Microdroplet Generation..... | 21        |
| 3.4.3 Optical Setup.....  | 22        |
| 3.5 Electrostatic Simulations with COMSOL <sup>®</sup> .....    | 23        |
| 3.6 Experimental Results.....                                   | 24        |
| 3.6.1 Nondegeneracy in WGMs.....                                | 24        |
| 3.6.2 Contact Angle Measurement.....                            | 28        |
| 3.7 Summary.....  | 31        |
| <br>  |           |
| <b>Chapter 4: Raman Lasing From Pure Water Microdroplets</b>    | <b>32</b> |
| 4.1 Introduction.....   | 32        |
| 4.2 Raman Scattering: Stokes and anti-Stokes Scattering.....    | 33        |
| 4.3 Raman Lasing Threshold.....                                 | 34        |
| 4.4 Sample Preparation and Experimental Setup.....              | 35        |
| 4.4.1 Superhydrophobic Coating and Microdroplet Generation..... | 35        |
| 4.4.2 Humidity Chamber.....                                     | 36        |
| 4.4.3 Optical Setup.....  | 37        |
| 4.5 Experimental Results.....                                   | 38        |
| 4.5.1 Raman Spectrum of Liquid Water.....                       | 38        |
| 4.5.2 Raman Lasing from Pure Water Microdroplets.....           | 39        |
| 4.6 Summary.....  | 43        |
| <br>  |           |
| <b>Chapter 5: Conclusion</b>                                    | <b>44</b> |
| <br>  |           |
| <b>Appendix</b>   | <b>46</b> |
| <br>  |           |
| <b>Bibliography</b>   | <b>59</b> |

## LIST OF TABLES

|  |    |
|--|----|
| Table 3.1 The recipe used in UV lithography and HCl wet etching..... | 20 |
|--|----|



## LIST OF FIGURES

|  |    |
|--|----|
| Figure 1.1: Deformed droplet towards prolate spheroid.....   | 3  |
| Figure 1.2: Raman lasing from pure water.....  | 3  |
| Figure 1.3: Spin coater.....   | 5  |
| Figure 1.4: Millimetric water microdroplet standing on a superhydrophobic surface has contact angle larger than $150^\circ$ .....  | 6  |
| Figure 1.5: a) Ultrasonic nebulizer, b) Microscope image of the microdroplets standing on a superhydrophobic surface.....  | 6  |
| Figure 2.1: a) WGMs are coupled to equatorial plane and they propagate along a zig-zag path around the sphere. b) TE-mode with mode numbers $n = 1$ and $l = 20$ .....   | 8  |
| Figure 2.2: MATLAB simulation of coupled WGMs, a) $l = 30, n = 0$ b) $l = 30, n = 15$ c) $l = 30, n = 30$ .....  | 12 |
| Figure 3.1: Fabrication flow: (a) Cover glass cleaning. (b) Spin coating of photoresist. (c) UV Photolithography. (d) Photoresist development. (e) Indium tin oxide layer on the surface is etched with HCl. (f) Photoresist stripped..... | 18 |
| Figure 3.2: Contact profile of the sample. Inset: UV lithography pattern of indium tin oxide contacts on cover glass.....  | 19 |
| Figure 3.3: Microscope image of the microdroplets standing between ITO contacts.....   | 21 |
| Figure 3.4: Experimental setup. G: cover glass; SH: superhydrophobic surface; ITO: indium tin oxide contacts. The dashed line shows the deformed microdroplet under the influence of the electric field.....                               | 22 |
| Figure 3.5: Optical setup.....   | 23 |
| Figure 3.6: Strength of the electric field through the distance between ITO contacts.....  | 24 |

|  |    |
|--|----|
| Figure 3.7: Consecutive normalized spectra recorded from a 5.2 $\mu\text{m}$ diameter microdroplet at different voltages. The dashed spectrum at 0 V was obtained after a full cycle of increasing and decreasing the voltage.....   | 25 |
| Figure 3.8: Electrical capillary dependence of the deformation. Solid line shows the theoretical curve and dashed line corresponds to experimental results.....  | 27 |
| Figure 3.9: High voltage spectra recorded from microdroplets 1 (a) and 2 (b). Isolated sharp peaks correspond to twofold degenerate WGMs. The well resolved peaks used in the analysis are indicated. Applied voltages and contact spacings are 350 V, 37 $\mu\text{m}$ and 320 V, 33 $\mu\text{m}$ for spectra 1 and 2, respectively..... | 28 |
| Figure 3.10: Measured peak positions are shown as squares (spectrum 1) and triangles (spectrum 2). Solid lines indicate the best fit curves. Inset: Error as a function of $h$ obtained by matching the separations between the selected peaks to the theoretical formula.....   | 29 |
| Figure 3.11: Contact angle histogram of glycerol-water microdroplets standing on a LE2 surface.....  | 30 |
| Figure 4.1: Different possibility of light scattering, Stokes scattering and anti-Stokes scattering.....   | 33 |
| Figure 4.2: Mini humidity chamber.....   | 36 |
| Figure 4.3: Optical Setup.....   | 37 |
| Figure 4.4: Raman spectrum of liquid water including resonances due to OH-stretching bonds.....  | 38 |
| Figure 4.5: Consecutive spectra recorded from a 13- $\mu\text{m}$ diameter water microdroplet during the (a) “off” and (b) “on” periods of Raman lasing.....   | 40 |
| Figure 4.6: Contour plot of a 13- $\mu\text{m}$ diameter microdroplet exhibiting Raman lasing. Momentary single-mode (acquisitions numbers 6, 13, 14 and 15) and multi-mode (acquisition number 10) Raman lasing is observed.....  | 41 |

Figure 4.7: Time trace of the Raman lasing intensity from a 14- $\mu\text{m}$  diameter microdroplet shows the “on/off” behavior. Inset: image used in calculating the time trace.....42

## NOMENCLATURE

|   |  |
|---|--|
| $WGM$                                     | whispering gallery mode                          |
| $LE$                                      | lotus effect                                     |
| $MDR$                                     | morphology-dependent resonance                   |
| $TE$                                      | transverse electric                              |
| $TM$                                      | transverse magnetic                              |
| $n$                                       | mode number                                      |
| $l$                                       | mode order                                       |
| $m(\omega)$                               | index of refraction                              |
| $\theta_{inc}$                            | angle of incidence                               |
| $\theta_c$                                | angle  |
| $\Psi$                                    | scalar field in spherical coordinates            |
| $k$                                       | wave number                                      |
| $\vec{E}_s, \vec{E}_{int}, \vec{E}_{inc}$ | scattered, internal and incident electric fields |
| $N_n^{(a)}, M_n^{(a)}$                    | vector spherical harmonic functions              |
| $z_n^a(kr)$                               | spherical Bessel function                        |
| $Y_n^l(\theta, \phi)$                     | spherical harmonics                              |
| $a_n, b_n, c_n, d_n$                      | Mie expansion coefficients                       |
| $FWHM$                                    | full width at half maximum                       |
| $\tau$                                    | lifetime of a wave                               |
| $r_p, r_e$                                | semimajor and semiminor axes of a spheroid       |
| $C_e$                                     | electrical capillary number                      |
| $\varepsilon$                             | permittivity of air                              |
| $\gamma$                                  | interfacial tension of air-glycerol              |
| $e$                                       | deformation amplitude                            |

|                        |  |
|------------------------|--|
| $ITO$                  | indium tin oxide                               |
| $NA$                   | numerical aperture                             |
| $N_0, N_1$             | number of atoms in the lower and higher states |
| $g_0, g_1$             | degeneracy of the states                       |
| $k_B$                  | Boltzmann's constant                           |
| $P_{thresh}$           | threshold pump power                           |
| $C(\Gamma)$            | circulating power correction factor            |
| $\lambda_p, \lambda_R$ | wavelengths of pump and Raman mode             |
| $g_R$                  | raman gain coefficient                         |
| $Q_0^P, Q_0^R$         | quality factors of pump and raman mode         |
| $K_P, K_R$             | coupling parameters of pump and raman mode     |
| $V_{eff}$              | effective pump mode volume                     |
| $E_p, E_R$             | energy density of pump and raman volume        |
| $P_R$                  | total raman output power                       |
| $\omega_R, \omega_p$   | excitation frequency of raman and pump mode    |

## Chapter 1

### INTRODUCTION

#### 1.1 Overview

Optical microcavities enable confinement of light into small volumes by resonant recirculation. They can modify the spatial distribution of radiation power, change the spectral width of the emitted light and enhance or suppress the spontaneous emission rate [1]. Microcavities are attractive for not only studying the interaction between materials and vacuum field fluctuations, but also constructing novel kinds of light emitting devices [1]. There are various geometries, which serve as optical microcavity; cylindrical, spherical, spheroidal/toroidal, ring and other shapes [2]. Using these geometries, Fabry-Perot resonators [3], microdiscs [4], microrings [5], microspheres [6], annular Bragg microcavities [7], microtoroids [8], micropillars [9], photonic crystal defect microcavities [10], and microdroplets [11] have been studied with various confining principles. Optical microcavities have many applications in cavity quantum electrodynamics, optoelectronics and biological sensing [12].

The effects of the discrete mode structures of a cavity are the main issue in cavity quantum electrodynamics [13]. These effects are modification of the spontaneous emission rate of a single atom and the energy levels of the atoms (Lamb shift) in an optical cavity, which occur in weak coupling between radiation and atom. On the other hand, oscillatory energy exchange between a single atom and the cavity mode requires strong coupling in the ideal situation. Thus, the applications in cavity quantum

electrodynamics depend on the coupling constants of the optical microcavities and the experiments are performed for very low threshold lasers.

Optical microcavities are also used as a component for optoelectronic devices. Due to their dimensions and high quality factors, microspheres with whispering gallery modes allows the creation of very small high-spectral purity sources in optical and microwave bands [14]. Coupling methods to fibers and waveguides are important for integration of the microspheres in functional devices.

Biological sensing is another area that benefits from the properties of optical microcavities. For example, a resonant microcavity with deformable coating such as a polymer is used for gas or vapor sensing [15]. The polymer coating expands when it absorbs a gas or vapor, which changes the resonant wavelength of the coated microcavity. As a result of the coating deformation and the resonant wavelength, the sensor detects the presence of the gas or vapor.

Liquid microcavities have taken attention because they provide relatively easy control of its shape due to their flexible nature. The size and shape changes can be controlled when the liquid microcavity is exposed to an external force or electric field. For example liquid lenses, in which the shape is controlled by electric field, have found technological applications [16]. Liquid droplets tend to minimize interfacial energy by minimizing the interfacial area, which results almost spherical shapes in air. Because of this property, they were used in various experiments such as suspending single liquid microdroplets in air by optical levitation [17]. In that work, they analyzed the laser power required for stabilization of the height of the microdroplets as a function of wavelength and they observed the whispering gallery modes [18]. There are various studies about characterization of the liquid microdroplets; tuning in WGMs [11], volume stabilization [19], dye lasing [20] were performed before.

In this thesis, observation of nondegenerate cavity modes in glycerol-water microdroplets deformed by a uniform electric field is discussed. In order to perform the experiments, we used a superhydrophobic surface, which increases the robustness of the experiments against external disturbances. A uniform electric field was applied by the

help of microfabricated electrical contacts. At high voltages, the shape of the microdroplet changes towards a prolate spheroid as shown in Figure 1.1.

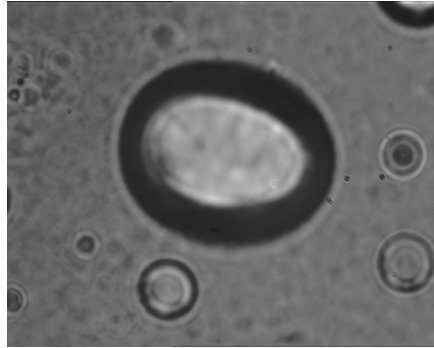


**Figure 1.1** A microdroplet deformed towards a prolate spheroid

Raman lasing near 650 nm (Figure 1.2) in isolated pure water microdroplets is also discussed in this thesis. Raman lasing from pure water microdroplets is important for developing novel organic light emitting devices because light sources emitting around 650 nm hold considerable importance for these systems.



**Figure 1.2** Raman lasing from pure water



## 1.2 Thesis Outline

Chapter 1 begins with the explanation of the superhydrophobic surface preparation, microdroplet generation and experimental setup.

In Chapter 2, cavity modes of microspheres are discussed. This chapter contains brief analytical solution of whispering gallery modes obtained by the help of ray and wave optics and the Mie theory. Quality factor of WGMs is also reviewed in this chapter.

Chapter 3 demonstrates the deformability of liquid microdroplets under a uniform electric field. Degeneracy in WGMs is lifted when the deformation occurs. Thus, this chapter includes not only the illustration of the deformation in liquid droplets, but also showing the nondegeneracy in WGMs. Contact angle measurement is another result in our experiments, which is also review in this chapter.

Chapter 4 includes the demonstration of Raman lasing from isolated pure water microdroplets standing on a superhydrophobic surface. Intense Raman emission from one dominant WGM with a high signal to noise ratio up to 25 dB is demonstrated in this chapter.

At the last chapter, results of our experiments are briefly reviewed.

### 1.3 Surface preparation and Microdroplet Generation

Commercial hydrophobically coated silica nanoparticles (Evonik/Degussa A.G., Aeroxide<sup>®</sup> LE1, LE2) are used to make superhydrophobic surfaces. These nanoparticles are solved in ethanol with an appropriate dispersion proportion to obtain microdroplets with high contact angle. Usually, 50 mg/ml ethanol dispersion of hydrophobically coated nanoparticle solution is used to prepare the superhydrophobic surface with spin coater (Fig.1.3) on a cover glass at 2000 rpm for 1 minute. In order to evaporate remaining solvent, resulting samples are post-baked in an oven at 80° for 15 minutes.



**Figure 1.3** Spin coater

Nanoparticles LE1 and LE2 have an average particle size diameter of 20 nm and 7 nm, respectively. However, during spin coating, nanoparticles aggregate and structures bigger than particle size occur on the surface. Resulting samples have nanoscale surface roughness and transparent to visible light. Average contact angle measurements are done with millimetric size water microdroplets to test the superhydrophobic surface. LE1 and LE2 surfaces do not give the same results but they have contact angle around 150° (Fig.1.4).

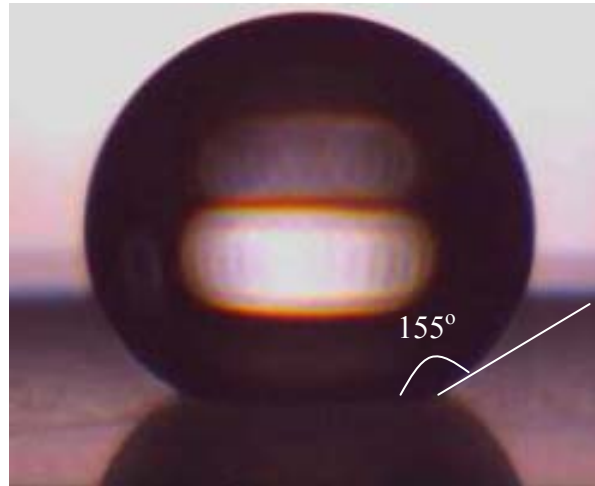


**Figure 1.4** Millimetric size water microdroplet standing on a superhydrophobic surface has contact angle larger than  $150^\circ$

Ultrasonic nebulizer is used to generate microdroplets with diameters ranging up to  $\sim 10 \mu\text{m}$  placed on the surface. For Chapter 4, we use pure water to generate microdroplets and for Chapter 3, Rhodamine B doped glycerol/water solution is generated using ultrasonic nebulizer shown in Figure 1.5 (a). Microscope image of glycerol/water microdroplets is shown in Figure 1.5 (b).

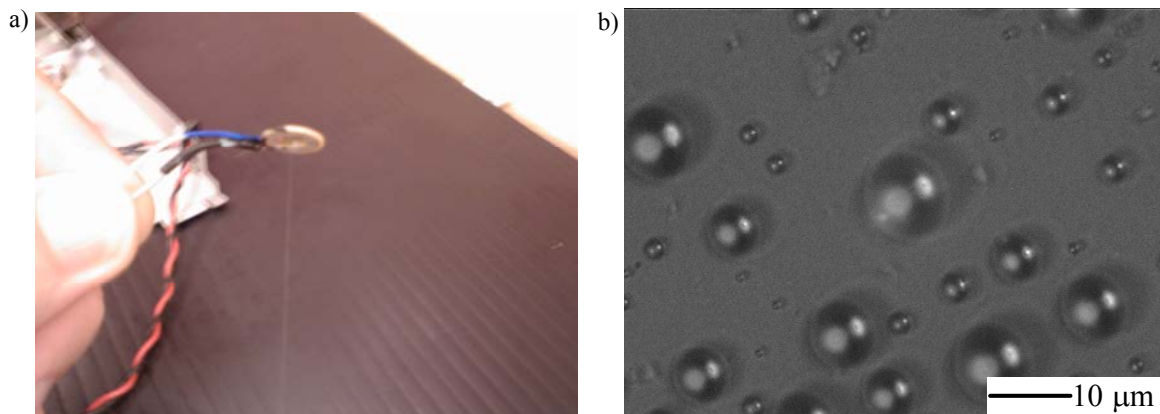


**Figure 1.5** (a) Ultrasonic nebulizer, (b) Microscope image of the microdroplets standing on a superhydrophobic surface.

## Chapter 2

### CAVITY MODES OF MICROSPHERES

#### 2.1 Introduction

Electromagnetic theory provides rigorous information about interaction of light with dielectric microspheres and it explains physical and mathematical properties of the resonance modes. Optical modes of a dielectric sphere can be calculated by Mie theory based on the arbitrary radius and refractive index of the sphere. Sharp peaks in the calculated spectrum of the electromagnetic wave could be attributed to resonant recirculation of optical energy which is called whispering gallery modes (WGMs) or morphology-dependent resonances (MDRs). Most of the optical properties of microspheres are associated with WGMs that are confined in three dimensions.

In this chapter, characteristic equations and properties of the WGMs will be discussed with the help of the book of Mitchell H. Fields [21]. We also summarize the Mie Theory formulation used by J.P. Barton [22]. Firstly, initial treatment to explore modes with ray and wave optics and then the complete description of the resonance modes will be briefly reviewed.

## 2.2 Whispering Gallery Modes (WGMs)

Whispering gallery mode resonances occur at particular resonant wavelength of light for a given cavity size. At these wavelengths, the light undergoes total internal reflection at the sphere surface and becomes trapped within the sphere. The modes are most strongly coupled along the equatorial plane and they propagate along a zig-zag path around the sphere as shown in Figure 2.1(a). WGMs are named after the whispering gallery at St. Paul's cathedral in London because of their similarity in the acoustic waves propagating around whispering gallery.

The solutions of Helmholtz equation show two linearly independent polarizations, transverse electric (TE) and transverse magnetic (TM) modes of WGMs. These modes are characterized by mode number  $n$ , which indicates the number of wavelengths around the circumference of the sphere, and the mode order  $l$ , shows the number of maxima in the radial dependence of the electromagnetic field within the sphere. An example simulation for TE-mode with mode numbers  $n = 1$  and  $l = 20$  is shown in Figure 2.1(b).

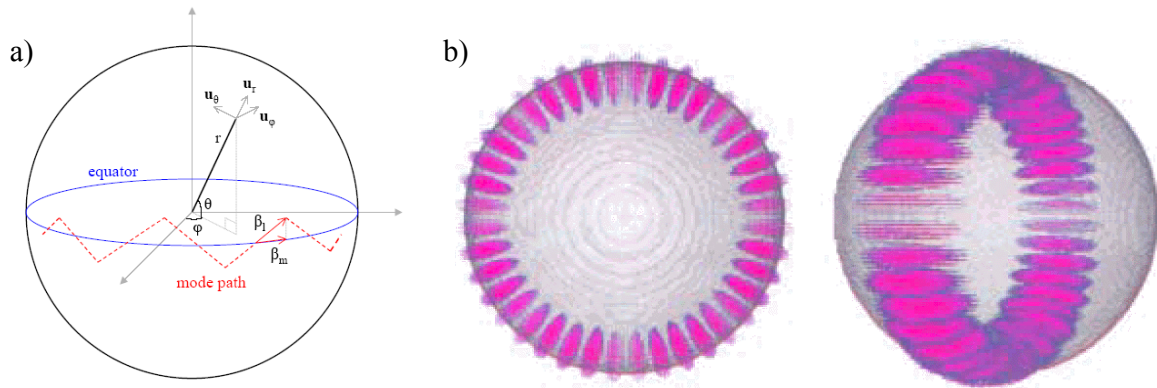


**Figure 2.1** (a) WGMs are coupled to equatorial plane and they propagate along a zig-zag path around the sphere. (b) TE-mode with mode numbers  $n = 1$  and  $l = 20$ .

The first explanation to optical resonances was based on ray and wave optics. However, it has several limitations in description of light interaction with a sphere. Complete description is given by Mie theory.

### 2.2.1 Ray and Wave Optics

The optical resonances of microspheres can be described by ray and wave optics, which particularize the manifestation of light. In the view of ray optics, the light is trapped inside the dielectric sphere by continuous total internal reflections at the curved boundary of surface. WGMs occur at discrete frequencies that depend on index of refraction  $m(\omega)$  and radius  $r$  of the sphere [21]. Total internal reflection occurs if the angle of incidence with the dielectric interface is

$$\theta_{inc} \geq \theta_c = \arcsin(1/m(\omega)). \quad (2.1)$$

The rays of a mode have the property that all subsequent bounces have the same angle of incidence. Dielectric sphere has an inner-sphere region, which is called ‘caustic region’ where the propagating bouncing rays are tangent. Caustic sphere has a radius defined by a ray with  $\theta_{inc} \approx \theta_c$ , which is approximately the radial distance to a cord.

For a sphere with circumference  $2\pi r \gg \lambda$  and light propagating with  $\theta_{inc} \approx 90^\circ$ , optical path length is approximately equal to the circumference of the sphere in the resonance condition. The path length for one roundtrip with waves confined mostly within the dielectric ( $\lambda/m(\omega)$ ) or extended into the surrounding air ( $\lambda$ ) determines the permitted limits for  $n$  wavelengths in the dielectric. The resonance condition occurs for integer  $n$  in the range,

$$\frac{2\pi a}{\lambda} \leq n \leq \frac{2\pi a}{\lambda/m(\omega)}. \quad (2.2)$$

The orbit of the rays is not always confined to the equatorial plane. If there is an angle  $\theta$  between the orbit and z-axis, the z-component of the angular momentum of the mode becomes  $m = n \cos \theta$ . All of the  $m$  modes have  $2n+1$  degeneracy for a perfect sphere. When the cavity is deformed from sphericity along z-axis, the degeneracy is lifted and nondegenerate modes can be seen. Resonance modes are independent of the circulation direction, so the integer  $m$  takes the values between  $[-n, +n]$ .

Ray and wave optics has some limitations in description of light interaction with a microsphere. First one is that characteristic leakage rates cannot be calculated by ray and wave optics and it does not provide possibility to couple of incident light into a WGM. Furthermore, the polarization of light is not taken into account. Ray and wave optics cannot be used to determine the radial character of the modes. Maxwell wave equations can resolve these problems with appropriate boundary conditions.

### 2.2.2 Mie Theory: Light Scattering of a Dielectric Sphere

Maxwell equations are used to derive a wave equation for electromagnetic radiation in three dimensional space and these are expressed in spherical coordinates with appropriate boundary conditions at the surface of the sphere. Mie theory provides us a general solution to the boundary value problem in vector spherical harmonics by separating the incident, scattered and internal electromagnetic fields [22] and satisfying the Helmholtz equation.

$$\begin{aligned}\nabla^2 \vec{E} + k^2 \vec{E} &= 0, \\ \nabla^2 \vec{H} + k^2 \vec{H} &= 0,\end{aligned}\tag{2.3}$$

where  $\vec{E}$  and  $\vec{H}$  are electric and magnetic fields, respectively and  $k$  is wave number. These vector equations can be converted into scalar equations. For instance, for the electric field and magnetic fields, we define the potential  $\Psi$  as

$$\begin{aligned}\vec{E}_{mn} &= \nabla \times \vec{r} \Psi_{mn}, \\ \vec{H}_{mn} &= \frac{1}{k} \nabla \times \nabla \times \vec{r} \Psi_{mn}.\end{aligned}\quad (2.4)$$

where  $\vec{r}$  is the position vector. Equation (2.4) can be substituted into equation (2.3) to obtain

$$\nabla^2 \Psi + k^2 \Psi = 0 \quad (2.5)$$

which is a scalar field and can be solved by standard techniques [22]. Sum over the vector spherical harmonics gives the general solution to the scattered, internal and incident electric fields.

$$\begin{aligned}\vec{E}_s &= \sum_{n=1}^{\infty} E_n \left[ ia_n \vec{N}_{eln}^{(3)} - b_n \vec{M}_{oln}^{(3)} \right], \\ \vec{E}_{int} &= \sum_{n=1}^{\infty} E_n \left[ c_n \vec{M}_{oln}^{(1)} - id_n \vec{N}_{eln}^{(1)} \right], \\ \vec{E}_{inc} &= E_0 \sum_{n=1}^{\infty} i^n \frac{2n+1}{n(n+1)} \left[ \vec{M}_{oln}^{(1)} - i \vec{N}_{eln}^{(1)} \right],\end{aligned}\quad (2.5)$$

where  $o$  and  $e$  refers to odd and even multipoles, respectively and  $a$ ,  $b$ ,  $c$  and  $d$  are expansion coefficients. There are similar solutions for the magnetic fields. The vector spherical harmonic functions are defined as

$$\begin{aligned}N_n^{(a)} &= \frac{1}{k} \nabla \times \nabla \times \left( \vec{r} z_n^a(kr) Y_n^l(\theta, \phi) e^{if} \right), \\ M_n^{(a)} &= \nabla \times \left( \vec{r} z_n^a(kr) Y_n^l(\theta, \phi) e^{if} \right),\end{aligned}\quad (2.6)$$

here,  $z_n^a(kr)$  is spherical Bessel functions standing for  $j_n(kr)$ ,  $h_n^{(1)}(kr)$  and  $h_n^{(2)}(kr)$  of order  $n$ .  $Y_n^l(\theta, \phi)$  is the spherical harmonics.  $l$  is the mode order, which gives the number of maxima in the radial dependence and  $n$  is the mode number that gives the number of maxima in the angular dependence between 0 and 180°. 3D color plots of coupled



WGMs with  $l=30$  and different  $n$  values are shown in Figure 2.2. The mode number also specifies the order of the Bessel functions that constitute the radial part of the WGM.

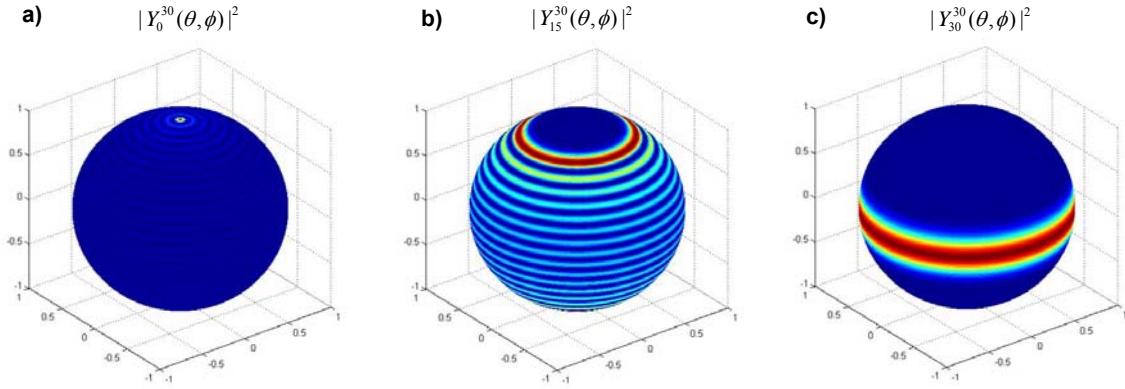


**Figure 2.2** MATLAB simulation of coupled WGMs (a)  $l = 30$ ,  $n = 0$  (b)  $l = 30$ ,  $n = 15$  (c)  $l = 30$ ,  $n = 30$

The Mie expansion coefficients  $a_n$ ,  $b_n$ ,  $c_n$  and  $d_n$  are defined same for any incident laser beam mode;

$$\begin{aligned}
 a_n &= -\frac{j_n(mx)[xj_n(x)]' - [mxj_n(mx)]'j_n(x)}{j_n(mx)[xh_n^{(1)}(x)]' - [mxj_n(mx)]'h_n^{(1)}(x)}, \\
 b_n &= -\frac{m^2 j_n(mx)[xj_n(x)]' - [mxj_n(mx)]'j_n(x)}{m^2 j_n(mx)[xh_n^{(1)}(x)]' - [mxj_n(mx)]'h_n^{(1)}(x)}, \\
 c_n &= \frac{j_n(mx)[xh_n^{(1)}(x)]' - [xj_n(x)]'h_n^{(1)}(x)}{j_n(mx)[xh_n^{(1)}(x)]' - [mxj_n(mx)]'h_n^{(1)}(x)}, \\
 d_n &= m \frac{j_n(x)[xh_n^{(1)}(x)]' - [xj_n(x)]'h_n^{(1)}(x)}{m^2 j_n(mx)[xh_n^{(1)}(x)]' - [mxj_n(mx)]'h_n^{(1)}(x)},
 \end{aligned} \tag{2.7}$$

where  $x$  is called size parameter equals to  $x = 2\pi a / \lambda$ ,  $a$  is the radius of the sphere and  $m$  is the refractive index of the scattering medium. The primes in the equations refer to differentiation with respect to the arguments.

From the equation (2.7), the conditions of the resonance modes of  $n$ th mode electric and magnetic wave can be achieved by setting the denominator to zero. These modes ( $TM$  and  $TE$ ) are characterized by whether  $a_n$  or  $b_n$  are dominant to each other. For  $TM$  modes,  $a_n$  is dominant;

$$\frac{[mxj_n(mx)]'}{[mj_n(mx)]} - m^2 \frac{[xh_n^{(1,2)}(x)]'}{[h_n^{(1,2)}(x)]} = 0, \quad (2.8)$$

when  $b_n$  is dominant, we get the  $TE$  mode;

$$\frac{[mxj_n(x)]'}{[j_n(x)]} - \frac{[xh_n^{(1,2)}(x)]'}{[h_n^{(1,2)}(x)]} = 0. \quad (2.9)$$

### 2.2.3 Quality Factor (Q) in WGMs

The quality factor of a cavity is defined as the ratio of the resonance frequency to the width of the resonance curve. The real part of the size parameter  $x$  is related to the resonance frequency by  $\omega = c \operatorname{Re}(x) / a$ . The full width at half maximum (FWHM) of the resonance mode  $\Delta\omega$  is twice the imaginary part of  $x$ . The quality factor (Q) of a resonance is defined as [21]

$$Q = \frac{\operatorname{Re}(x)}{2 \operatorname{Im}(x)} = \frac{\omega}{\Delta\omega} = \omega\tau, \quad (2.10)$$

where  $\tau$  is the lifetime of a wave on a WGM. For a perfect, lossless sphere condition, diffractive leakage losses set limits in Q-values which can be as high as  $10^{100}$ . However, this high quality value can not be reachable because of volume inhomogeneities, surface roughness and absorption. These restrictions cause the maximum Q-values to be less than  $10^{10}$ . Other effects such as shape deformations and nonlinear effects can also reduce the maximum Q-values.

## Chapter 3

### CONTROLLED OBSERVATION OF NONDEGENERATE CAVITY MODES IN A MICRODROPLET

#### 3.1 Introduction

Liquid microdroplets can easily be deformed by external forces due to its flexible nature [23]. Without any disturbances, glycerol-water microdroplets standing on a superhydrophobic surface take the shape of a truncated microsphere. WGM solutions of an ideal truncated dielectric sphere and an ideal dielectric sphere are similar because their spectral positions are same in the resolution of our experiments [24]. WGMs with the same polarization, radial mode order, and angular momentum number are  $2l+1$  degenerate for an ideal dielectric sphere. In consequence of the deformation of a liquid microdroplet, the azimuthal degeneracy of the WGM is lifted so that WGM solutions for an ideal case and truncated case become apparent. In this chapter, the experiments rely on the deformation of microdroplets towards a prolate spheroid using a uniform electric field applied parallel to the superhydrophobic surface [25]. It is observed that there are fewer azimuthal modes than expected from an ideal spherical microdroplet. This difference is relevant to the truncated geometry, since the truncation prevents the propagation of the WGMs that cross the solid-liquid interface. The difference between the expected and observed number of azimuthal modes can be used to estimate the contact angle of the microdroplets [25].

### 3.2 Liquid Droplet Deformation in DC Electric Field

An isolated conducting liquid droplet is elongated a nearly prolate spheroid in the presence of a uniform electric field. Deformation is reversible and usually defined as [26]

$$D = \frac{(r_p - r_e)}{(r_p + r_e)} \approx \frac{(r_p - r_e)}{2r_0}, \quad (3.1)$$

where  $r_0$  is the initial radius of the droplet,  $r_p$  and  $r_e$  are the semimajor and semiminor axes of the spheroidal droplet parallel and perpendicular to the applied electric field, respectively. If the liquid droplet is deformed in the direction of the electric field, shape of the droplet becomes prolate spheroid and the resulting deformation is  $D > 0$ . On the other hand, if the liquid droplet is deformed in the direction perpendicular to the electric field, shape of the droplet becomes oblate spheroid and in this case  $D < 0$  [26].

For a glycerol microdroplet surrounded by air, electric force occurs normal to the air-glycerol interface because of the discontinuity in the electric stress [26]. Interfacial tension can be considered as a balancing force opposed to the electric field that tends to keep the shape of the droplet spherical. Elongation in the direction of the electric field occurs when the electric force overcomes interfacial tension. The magnitude of this interaction between electric force and interfacial tension is called electrical capillary number  $C_e$  and it is defined by an equation proportional to the square of the electric field strength as

$$C_e = \frac{r_0 \varepsilon E^2}{\gamma}, \quad (3.2)$$

where  $r_0$  is the radius of the droplet,  $\varepsilon$  is permittivity of air and  $\gamma$  is the interfacial tension of air-glycerol. According to the leaky dielectric model, small deformation and electrical capillary number is related by [26]

$$D = \frac{9}{16(2R+1)^2} \left[ (1+R^2 - 2PR^2) + 3R(1-PR) \frac{2+3V}{5+5V} \right] C_e. \quad (3.3)$$

Here  $R$ ,  $P$  and  $V$  are resistivity, permittivity and viscosity ratios of droplets to the surrounding air, respectively. Since the conductivity of air is too small ( $c_{\text{air}} \ll 1$ ), in our experiments  $R \rightarrow 0$  and deformation reduces to

$$D = \frac{9}{16} C_e. \quad (3.4)$$

Thus, for small elongation, magnitude of the deformation is linearly proportional to the electrical capillary number.

### 3.3 Azimuthal Degeneracy in WGMs

Resonance modes (WGMs) of an ideal sphere are described by the vector spherical harmonics and spherical Bessel functions labeled by radial mode order  $n$ , angular momentum number  $l$ , and azimuthal mode number  $m$  ranging between  $[l, -l]$ . For an ideal dielectric sphere with a certain angular momentum number  $l$ ,  $m$ -mode WGM has  $(2l+1)$  azimuthal degeneracy [27].

Each of the  $(2l+1)$ -degenerate WGMs has different frequency values and it forms  $(l+1)$  spectrally distinct WGMs. For each  $l, m$  mode, there is a different average radius and resonance frequency that is given by [27]

$$\omega(m) = \omega_0 \left\{ 1 - \frac{e}{6} \left[ 1 - \frac{3m^2}{l(l+1)} \right] \right\}, \quad (3.5)$$

where  $\omega_0$  is the frequency of the degenerate WGM of the microsphere and  $e$  is the deformation amplitude defined as

$$e = \frac{r_p - r_e}{r_0} \quad \begin{array}{l} e > 0 : \textit{prolate} \\ e < 0 : \textit{oblate} \end{array} \quad (3.6)$$

For small deformations,  $D$  and  $e$  are related as

$$D \approx \frac{e}{2}. \quad (3.7)$$

Deformation is determined by the spectral spacing between the WGM with  $m=0$ , which is located approximately at the middle point of the highest wavelength hill in the spectrum, and the WGM with highest  $|m|$ . For large  $l$ ,

$$\begin{aligned} \omega(0) &\approx \omega_0 \left[ 1 - \frac{e}{6} \right], \\ \omega(l) &\approx \omega_0 \left[ 1 + \frac{e}{3} \right]. \end{aligned} \quad (3.8)$$

Thus, from the spectral spacing, we can find the deformation magnitude by

$$D \approx \frac{\Delta\lambda}{\lambda_0}. \quad (3.9)$$

### 3.4 Sample Preparation and Experimental Setup

#### 3.4.1 Fabrication process of the indium tin oxide contacts

Microfabrication process of indium tin oxide (ITO) contacts is performed for this experiment. Fabrication flow is shown in Figure 3.1. Commercial ITO coated cover glasses were cleaned up to get rid of any dust or residual particles and blown dry with N<sub>2</sub> gas. Wafer was then covered with positive photoresist by spinner. Resulting photoresist thickness on indium tin oxide coating was about 2 μm. Photoresist coated wafer was then soft-baked to drive off excess solvent and provide better adhesion to the surface, at 110 °C for 10 minutes on a hot plate.

The mask consisted of transparent and opaque regions that define the contact geometry. UV lithography was used for the contact preparation. Photoresist is sensitive to UV light, so when the wafer is exposed to UV light, chemical composition of the positive photoresist changes and becomes soluble in a developer. Contact features were obtained by developing the substrate with AZ 400K<sup>®</sup> developer. In the last step, ITO contacts were obtained by etching the indium tin oxide with isotropic HCl wet etching. The remaining photoresist was stripped by AZ 100<sup>®</sup> remover.

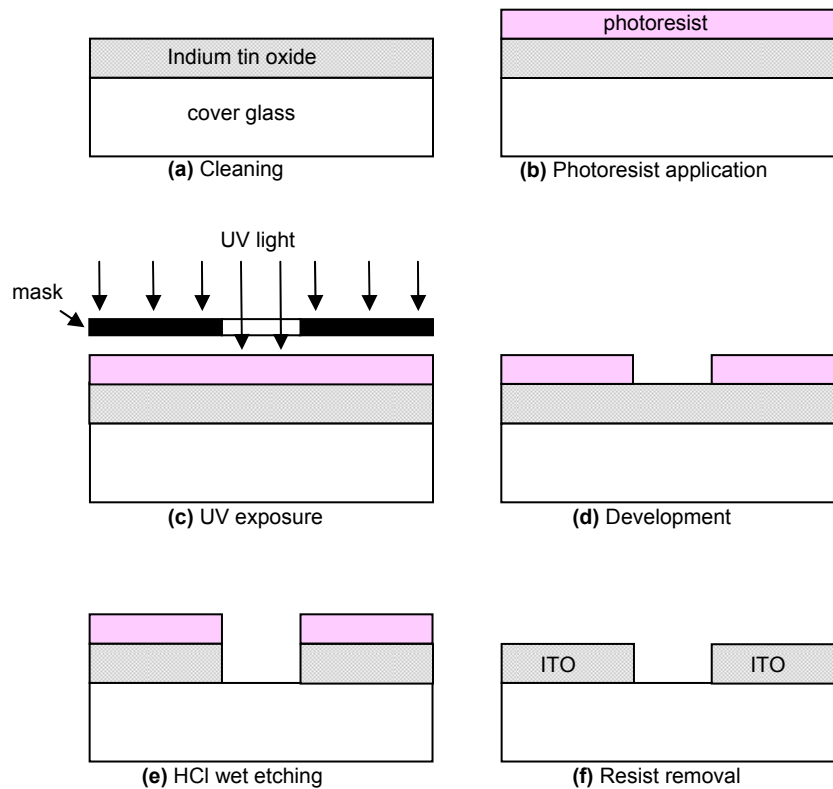


**Figure 3.1** Fabrication flow: **(a)** Cover glass cleaning. **(b)** Spin coating of photoresist. **(c)** UV Photolithography. **(d)** Photoresist development. **(e)** Indium tin oxide layer on the surface is etched with HCl. **(f)** Photoresist stripped

The quality of contact definition is based on the thickness of the resist, UV exposure time and development time. The thickness of the indium tin oxide layer on the cover glass was not uniform that causes non-ideal contact profile as shown in Figure 3.2.

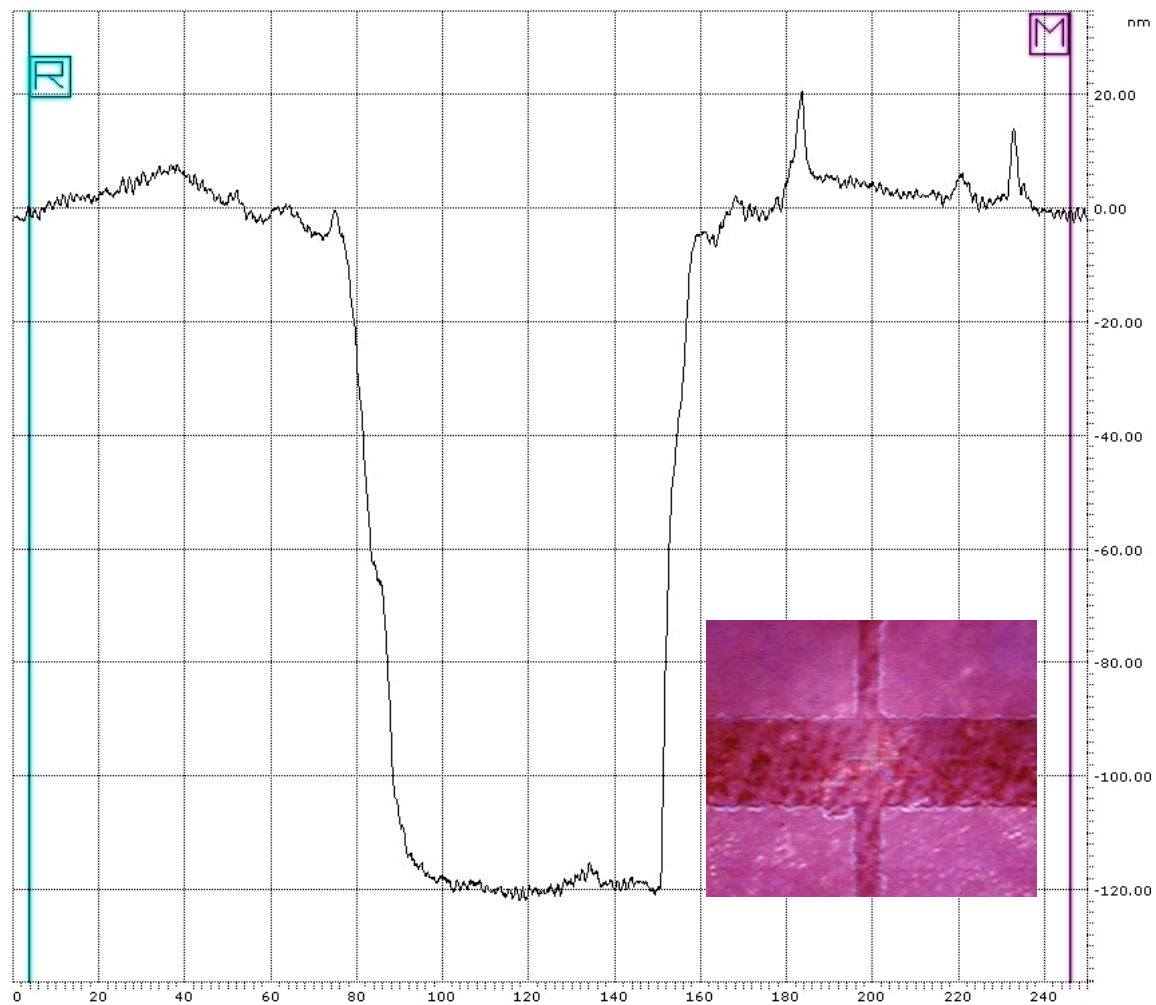


**Figure 3.2:** Contact profile of the sample. Inset: UV lithography pattern of indium tin oxide contacts on cover glass.



In fact, contact profile was not so much important since the two ITO contacts were separated completely. The thickness of indium tin oxide layer was approximately 120 nm. HCl wet etching time was optimized to dissolve indium tin oxide with thickness 120 nm. The full recipe for this process is given in Table 3.1.

| <b>Photolithography &amp; Etching Variable</b> | <b>Recipe</b>  |
|--|--|
| Photoresist type                               | Positive photoresist: AZ 5214  |
| Spin coating                                   | 1.6 $\mu\text{m}$ photoresist coating at 3000 rpm for 20 seconds and 5000 rpm for 30 seconds |
| Softbake                                       | 10 minutes at 110 °C   |
| Mask type                                      | Positive mask  |
| Exposure type                                  | Proximity exposure   |
| UV exposure dose                               | 40 seconds   |
| Development solution                           | 1:2 AZ 400K developer and DI water solution  |
| Development time                               | 20 seconds to 1 minute   |
| HCl concentration                              | Merck HCl 37%  |
| HCl etching time                               | 5 minutes or until full etching is obtained  |

**Table 3.1** The recipe used in UV lithography and HCl wet etching

### 3.4.2 Superhydrophobic Coating and Microdroplet Generation

Indium tin oxide contacts separated by around  $35\ \mu\text{m}$  were coated by hydrophobically coated silica nanoparticles (LE2) as discussed in Chapter 1. The resulting superhydrophobic surfaces were transparent to visible light and contain a nanoscale surface. Ultrasonic nebulizer was used to generate microdroplets with diameters ranging up to  $\sim 10\ \mu\text{m}$ . Percentage of glycerol-water solution was critical, because the ultrasonic nebulizer cannot generate microdroplets using just glycerol because of its viscosity. The maximum rate, which is 10/90 volume fraction of glycerol-water solution with  $2\ \mu\text{m}$  Rhodamine B dye molecules, was used to generate the microdroplets [25]. Glycerol-water microdroplets standing between two ITO contacts are shown in Figure 3.3.

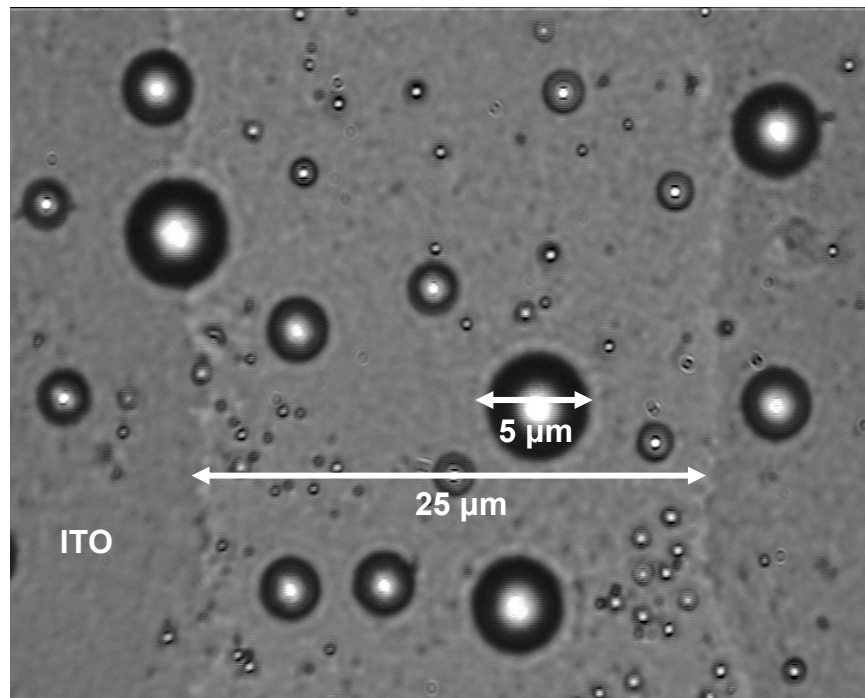


**Figure 3.3** Microscope image of the microdroplets standing between ITO contacts

After their generation, glycerol-water microdroplets quickly evaporated and reach their equilibrium sizes determined by the relative water humidity in the ambient atmosphere, which was  $62 \pm 5\%$  in this experiment. The equilibrium volume fraction of glycerol to water was then 65/35 [25]. The optical experiments were performed within 1-2 hours after microdroplet generation. Size reduction due to glycerol evaporation was observed during one day period using microscope images. However, this condition was predicted as  $<1\%$  size reduction, which did not effect our experiments significantly [25].

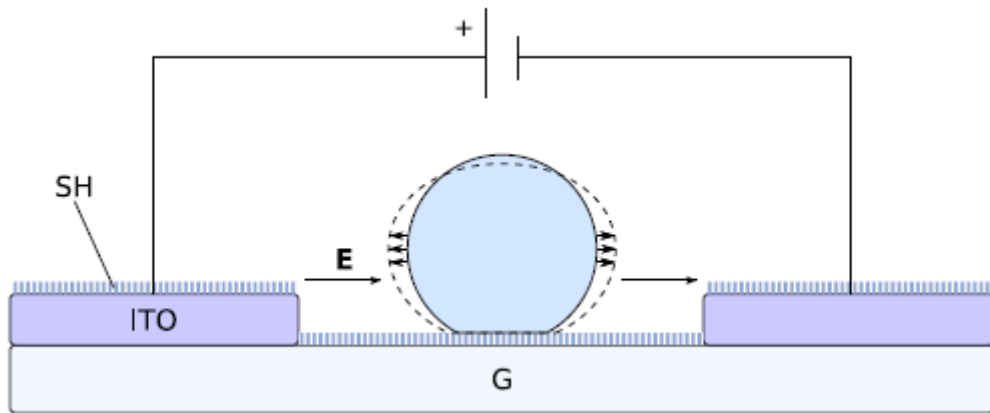


**Figure 3.4** Experimental setup. G: cover glass; SH: superhydrophobic surface; ITO: indium tin oxide contacts. The dashed line shows the deformed microdroplet under the influence of the electric field.

### 3.4.3 Optical Setup

In the optical setup, individual microdroplets were excited with a continuous wave solid state green laser ( $\lambda=532$  nm) using a microscope objective (NA=0.80, 60x) in the inverted geometry. Excitation powers at the focus of the microscope objective varied between 1 and 10  $\mu\text{W}$ . Fluorescence was collected with the same microscope objective, dispersed with a 50 cm monochromator (spectral resolution: 0.07 nm), and detected with a CCD camera using 1-3 s exposure times.

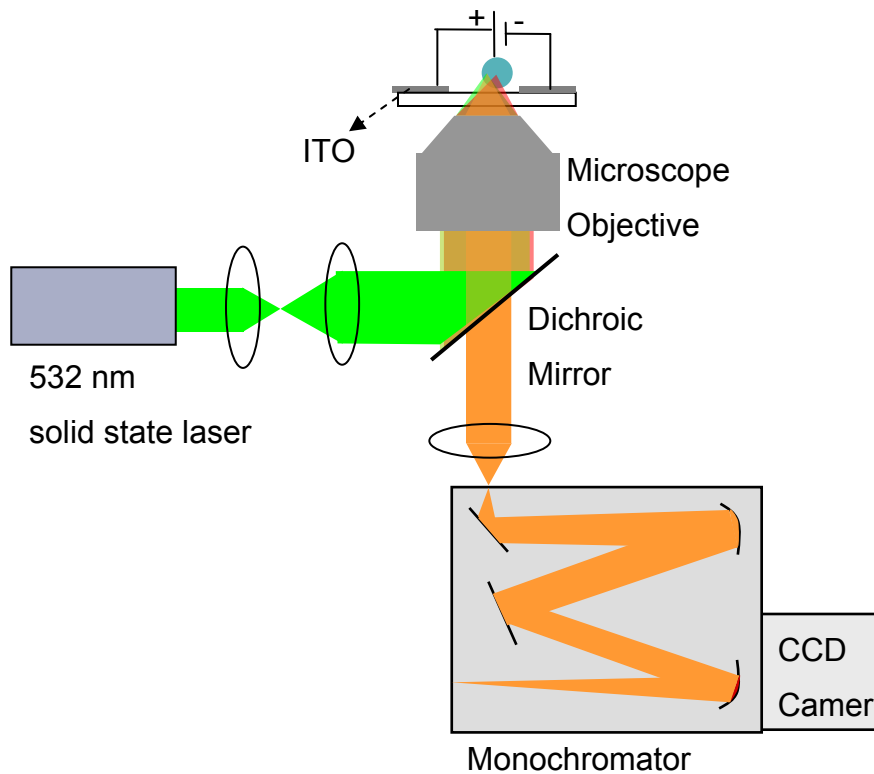


**Figure 3.5** Optical setup

### 3.5 Electrostatic Simulations with COMSOL<sup>®</sup>

We used microdroplets standing between two contacts with diameter ranging between 4-7  $\mu\text{m}$  but the thickness of indium tin oxide contacts (about  $\sim 120$  nm) was very small if we compare it with the microdroplet diameter. Because of this difference between the diameter and the thickness of the contacts, generated electric field would not be uniform every point of the microdroplet. In order to estimate the generated electric field along the center of the microdroplet, electrostatic simulations were performed with COMSOL<sup>®</sup>.

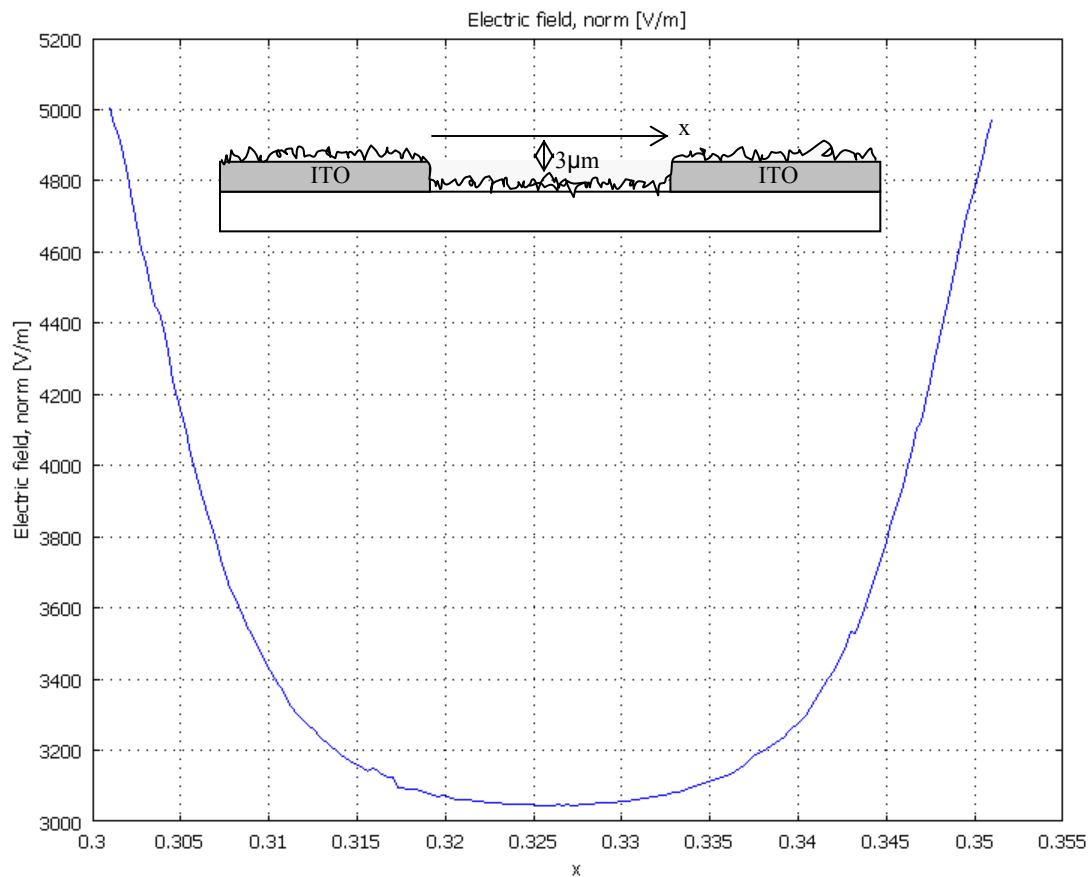


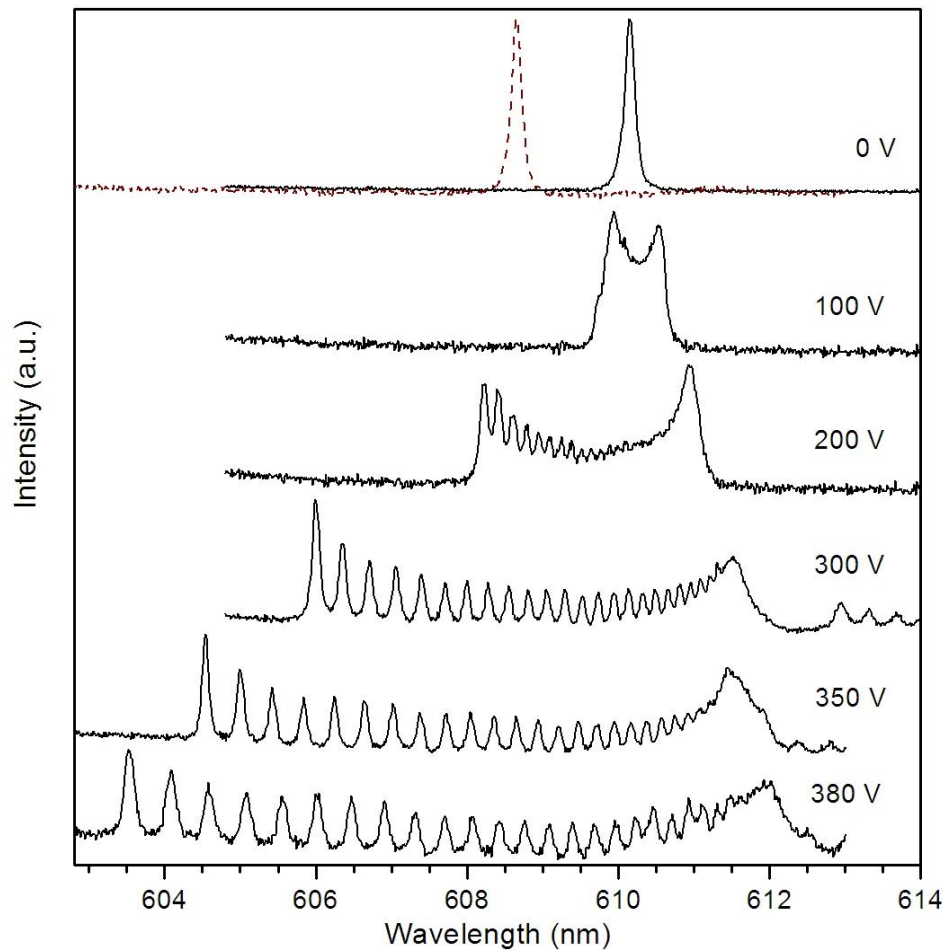
**Figure 3.6** Strength of the electric field through the distance between ITO contacts at the centerline.

### 3.6 Experimental Results

#### 3.6.1 Nondegeneracy in WGMs

Nondegenerate cavity modes were observed during the application of the voltage through the ITO contacts. In Figure 3.7, consecutive normalized spectra shows the nondegenerate WGMs recorded from a 5.2 μm diameter microdroplet as voltage applied between the contacts is first increased from 0 to 380 V, and then decreased back to 0 V. Concentration of the Rhodamine B dye molecules in the microdroplets put limit of ~50

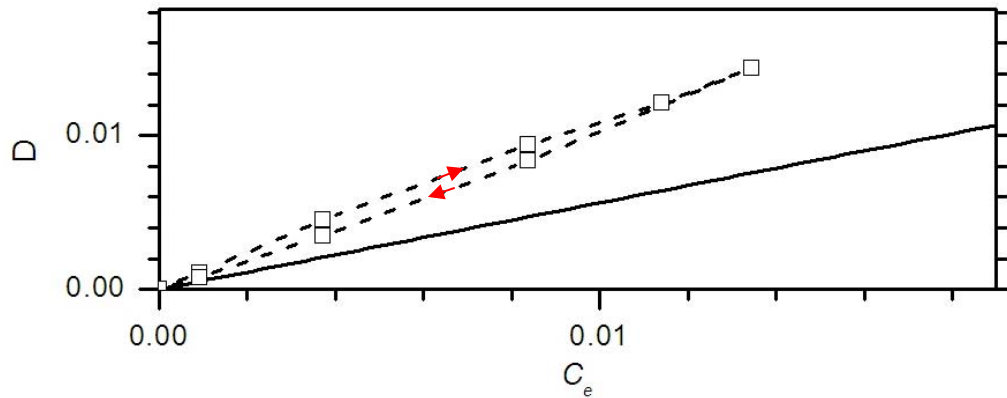
on the total number of spectra that could be recorded from a microdroplet because of photobleaching. However, our experiments were not influenced by this limitation because we did not need to take many spectrums.



**Figure 3.7** Consecutive normalized spectra recorded from a 5.2  $\mu\text{m}$  diameter microdroplet at different voltages. The dashed spectrum at 0 V was obtained after a full cycle of increasing and decreasing the voltage.

Before applying the electric field, azimuthally degenerate WGMs with same polarization, radial mode order and angular momentum number were observed in the spectra as shown in the first spectrum at 0 V of Figure 3.7. The single peak in this spectrum started to split as the voltage applied between the ITO contacts increased. After a full cycle of increasing and decreasing voltage, the dashed spectrum with same line shape was recorded at 0 V, which shows the controlled nature of the deformation scheme we present here. There is a slight blue shift of the dashed spectrum with respect to the solid spectrum, which shows the evaporation of the glycerol/water microdroplets during the experiment caused mainly by laser heating. This shift corresponds to decrease in the microdroplet size by 0.24%. These evaporation levels still enable tracking of the specific WGM between consecutive spectra, hence allowing for the analysis of its degeneracy lifting.

With the applied voltage, the azimuthal degeneracy between the WGMs is lifted, and well-resolved peaks were observed, especially in the low wavelength regime of the spectrum. In agreement with a deformation towards a prolate spheroid, each peak is twofold degenerate (+ $m$ , - $m$ ), and the azimuthal mode numbers of the WGMs approach zero with increasing wavelengths.  $m=0$  corresponds to the WGM peaked on the equatorial plane and parallel to the surface. With an increase in  $|m|$  (decrease in wavelength), spatial profiles of the WGMs approach the solid-liquid interface. Microdroplets were excited near their centers; this is why we observed an increase in the relative intensity of the peaks at lower wavelengths for a high voltage spectrum. These excitation conditions allow for a clear determination of the lowest wavelength peak which is critical in the contact angle estimation.



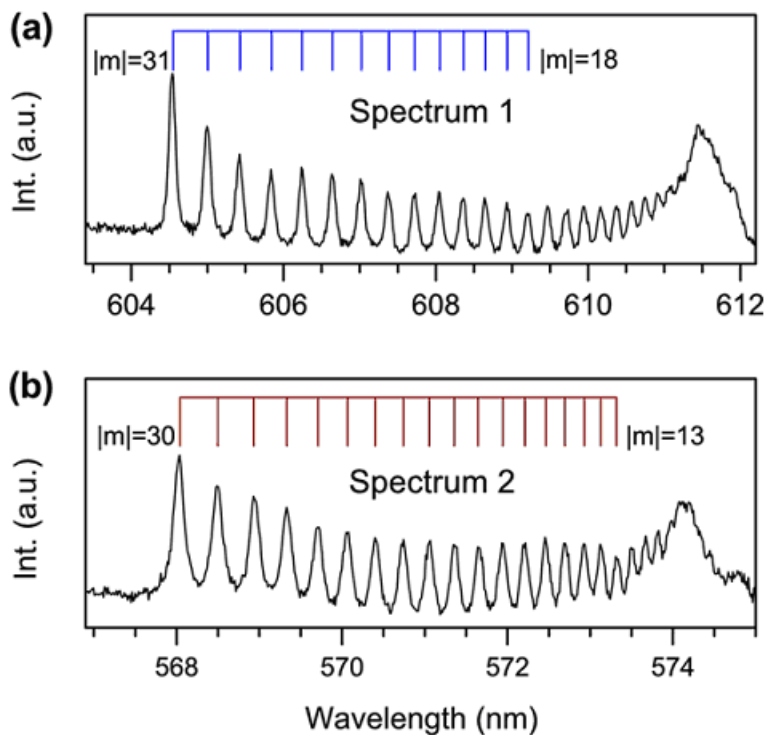
**Figure 3.8** Electrical capillary dependence of the deformation. Solid line shows the theoretical curve and dashed line corresponds to experimental results.

Figure 3.8 shows the change in the deformation  $D$  as a function of the electrical capillary number  $C_e$ . Deformation is determined by the spectral spacing between the WGM with  $m=0$  (located approximately at the middle point of the highest wavelength hill in the spectrum) and that having the highest  $|m|$  using  $\Delta\lambda/\lambda_0 \approx D$ , obtained from the equation 3.5 for large  $l$ . We obtained almost linear relationship between  $D$  and  $C_e$ , in agreement with the theoretical prediction. The difference between the theoretical and experimental slopes in Figure 3.8 is attributed to the presence of the superhydrophobic surface and a slight nonuniformity of the electric field.



### 3.6.2 Contact Angle Measurement

Lifting of the degenerate WGMs at high voltages give the relative locations of the peaks as shown in the Figure 3.9, which has detailed analysis of two different microdroplets with diameters of  $5.2\ \mu\text{m}$  (microdroplet 1) and  $5\ \mu\text{m}$  (microdroplet 2). In figure 3.9, isolated sharp peaks correspond to twofold degenerate WGMs. The contact spacing for spectra 1 and spectra 2 are  $37\ \mu\text{m}$  and  $33\ \mu\text{m}$ , respectively. The well resolved peaks were observed with the applied voltage  $350\ \text{V}$  for spectra 1 and  $320\ \text{V}$  for spectra 2.



**Figure 3.9** High voltage spectra recorded from microdroplets 1 (a) and 2 (b).

Determination of the peak locations is the first step for contact angle estimation. Peaks in the low  $|m|$  do not have a good spectral resolution. Thus, starting from the highest  $|m|$ , we identify a number of peaks with good spectral resolution for the analyses. 13 and 18 peaks are selected in spectra 1 and 2 in Figure 3.9. The spectral separation between the highest wavelength peak  $|m|=h$  and a given peak  $|m|=h+x$  is determined by the equation 3.5 as

$$\Delta\lambda(h, h+x) = \frac{-e\lambda_0}{[2l(l+1)]} [(h+x)^2 - h^2] \quad (3.10)$$

If we choose the lowest error value,  $h$ , shown in the inset of figure 3.10, the spectral separations between selected peaks that we got from our experiments are agree with the equation 3.10. We determined the value of  $h$  in this way and using the  $h$ ,  $|m|$  values of all the selected peaks were determined. As shown in Figure 3.10, our calculations fit very well with the experimental data. The linear dependence of  $\Delta\lambda$  on  $m^2=(h+x)^2$  is another justification for the deformation towards a prolate spheroid in our experiments.

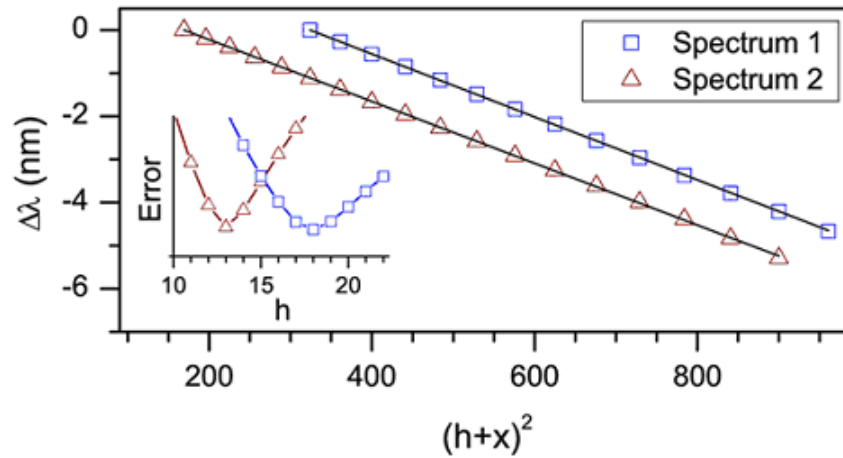


**Figure 3.10** Measured peak positions are shown for different microdroplets as squares (spectrum 1) and triangles (spectrum 2). Solid lines indicate the best fit curves. Inset: Error as a function of  $h$  obtained by matching the separations between the selected peaks to the theoretical formula.

For the spectra 1 and 2 in Figure 3.10, the lowest wavelength peaks are determined to have  $|m|$  values of 31 and 30, respectively. In order to estimate the contact angle, we compare these values with the expected angular momentum numbers  $l$ . The refractive index of the glycerol-water microdroplet was determined to be  $1.4210 \pm 0.0064$  at  $62 \pm 5\%$  relative humidity. From matching the theoretically expected WGM frequencies with three peaks spanning two free spectral ranges, the angular momentum numbers  $l$  were found for each microdroplet. For the high quality WGMs that we study (radial mode number  $n = 1$ ),  $l$  values are then determined as 34 and 32 for microdroplets 1 and 2, respectively. The radius of the microdroplets 1 and 2 are  $2.6 \mu\text{m}$  and  $2.5 \mu\text{m}$ , respectively.

In the experiments we have consistently observed maximum  $|m|$  values to be smaller than the expected  $l$  values for at least three other microdroplets. These differences are because of the contact with the surface, which has high refractive index prevents the confinement of the WGMs beyond a maximum  $|m_{\text{max}}|$  value. With simple geometry, contact angle can be estimated using the angular positions of the intensive maxima of the WGMs. With this method, contact angles are estimated to be  $160^\circ < \theta_1 < 164^\circ$  and  $164^\circ < \theta_2 < 170^\circ$  for microdroplets 1 and 2, respectively.

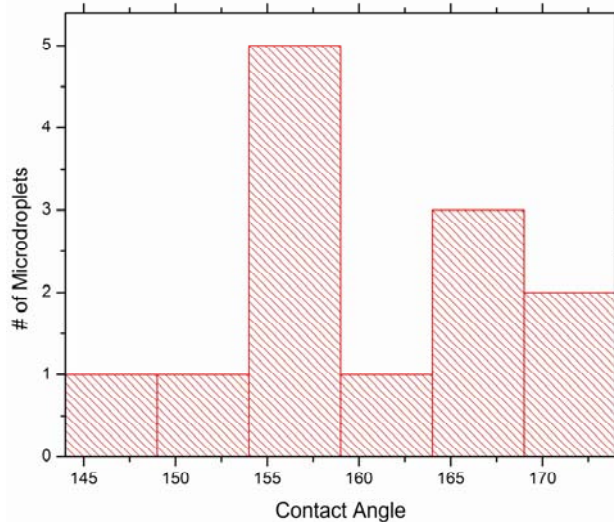


**Figure 3.11** Contact angle histogram of glycerol-water microdroplets standing on a LE2 surface

Figure 3.11 shows that most of the microdroplets standing on a LE2 surface have contact angles around  $155^\circ$ .

Contact angle estimation that we demonstrated here performed at high voltages. However, this method is also valid at low voltages due to relatively small deformations, and to the very little concentration of ions in the microdroplets which prevents electrowetting [28]. Our estimations are in agreement with the contact angle measurements performed on millimetric droplets using the specific superhydrophobic surface that we employ [29].

### 3.7 Summary

In this chapter, controlled lifting of the azimuthal degeneracy of the WGMs was demonstrated in glycerol-water microdroplets standing on a superhydrophobic surface by using a uniform electric field. Resolved nondegenerate WGMs were observed at high voltages. The relative locations of the resolved peaks were in good agreement with the deformation of the microdroplet towards a prolate spheroid. Our results reveal fewer azimuthal modes than expected from an ideal spherical microdroplet due to the truncation because of the droplet contact with the surface. We used this difference to estimate the contact angles of our microdroplets. Hence, the presented technique can be explored for the development of novel devices that measure the contact angles of microdroplets standing on a superhydrophobic surface. Stability condition can be improved in our experiments, for example salt-water microdroplets kept in humidity chamber can be used in future works. Stable condition can also provide us large tunable WGMs [30]. Our results can also inspire novel electrically tunable devices for applications in optoelectronics optofluidics. Using different electrical contact geometries, other fundamental studies on WGMs can also be studied.

## Chapter 4

### **RAMAN LASING FROM PURE WATER MICRODROPLETS STANDING ON A SUPERHYDROPHOBIC SURFACE**

#### **4.1 Introduction**

Optical microcavities enable confinement of light at the resonant frequencies to their small volumes. Liquid microdroplets standing on a superhydrophobic surface acts as a whispering gallery mode resonators and they are suitable for developing low threshold Raman lasers because of their high mode quality factors and small mode volumes [31]. They have found various applications, especially in developing novel organic light emitting devices suitable for low cost short-haul communication systems. Light sources emitting around 650 nm is significant requirement for these systems because of the low absorption of the plastic fibers [32]. Raman lasing obtained from pure water microdroplets is important in these applications, because photobleaching is not a limiting factor in these experiments and water microdroplet Raman lasers are organic light emitters [31].

In previous studies, Raman lasing has been demonstrated in both solid microspheres [33] and liquid microdroplets [34]. Different from the pervious works, Raman lasing near 650 nm in isolated pure water microdroplets located on a superhydrophobic surface is discussed in this chapter. Water microdroplets are pumped with a pulsed 532 nm laser. Different from the glycerol-water microdroplet work [34], in this study, we investigate isolated pure water microdroplets and our experimental configuration allows for recording Raman spectra of the microdroplets upon their excitation by many high-energy

laser pulses. Intense Raman emission was observed from one dominant WGM with a high signal to noise ratio up to 25 dB that provides strong indication of Raman lasing [31].

#### 4.2 Raman Scattering: Stokes and anti-Stokes Scattering

When light is scattered from an atom or molecule, most of the photons are elastically scattered with the same energy and wavelength as the incident photons, which is called Rayleigh scattering. However, some of the photons are inelastically scattered with different energy and usually lower than the energy of the incident photons, known as Raman scattering [35]. There are two types of Raman scattering, Stokes scattering and anti-Stokes scattering.

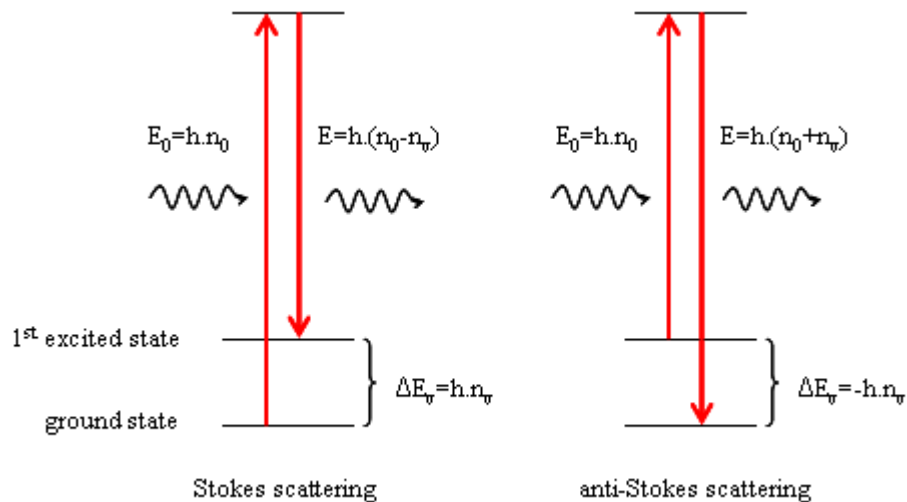


**Figure 4.1** Different possibility of light scattering, Stokes scattering and anti-Stokes scattering

The molecule is excited to a virtual energy level by absorbing a photon with energy  $E_0 = h.v_0$ . The molecule returns to the first excited state and emits the energy difference as a photon with lower energy  $E = h.(v_0 - v_v)$ . The radiation with lower energy (higher

wavelength) is called Stokes scattering [35]. The resulting photon with lower energy generates a Stokes line on the red side of the incident spectrum. In anti-Stokes scattering, the molecule is excited to a virtual energy level from the first excited state by absorbing a photon with energy  $E_0=h\nu_0$ . The molecule relaxes and returns to the ground state with emitting a photon with higher energy  $E=h(\nu_0+\nu_v)$ . Thus, incident photons are shifted to the blue side of the spectrum and generating an anti-Stokes line.

If the sample is in thermal equilibrium, the relative numbers of the molecules in different energy levels is given by Boltzmann distribution [35],

$$\frac{N_1}{N_0} = \frac{g_1}{g_2} e^{-\frac{\Delta E_v}{k_B T}} \quad (4.1)$$

where  $N_0$  and  $N_1$  are the number of atoms in the lower state and in the higher state, respectively.  $g_0$  and  $g_1$  are the degeneracy of the states and  $k_B$  is the Boltzmann's constant. According to equation 3.1, lower energy states have more molecules than higher energy states. Therefore, Stokes spectrum is more intense than anti-Stokes spectrum [35].

### 4.3 Raman Lasing Threshold

In an optical microcavity, Raman lasing starts when the cavity round-trip gain is in excess of round trip loss. The threshold for first-order Raman scattering is derived by steady-state solution of the coupled-mode equations [36]. Threshold pump power for stimulated Raman scattering depends on modal volume, coupling dependence and the Q factors of the Raman and pump modes [36].

$$P_{thresh} = C(\Gamma) \frac{\pi^2 n^2}{\lambda_p \lambda_R g_R} V_{eff} \left( \frac{1}{Q_0} \right)_P \left( \frac{1}{Q_0} \right)_R \frac{(1+K_P)^2}{K_P} (1+K_R) \quad (4.2)$$

where  $C(\Gamma)$  is the circulating power correction factor,  $\lambda_p$  and  $\lambda_R$  are the wavelengths of pump and Raman mode,  $g_R$  is the Raman gain coefficient,  $Q_0^P$  and  $Q_0^R$  are the quality factors of the pump and Raman mode,  $K_p$  and  $K_R$  are coupling parameters of pump and Raman mode.  $V_{eff}$  is the effective pump mode volume, which is defined as [36]

$$V_{eff} = \frac{\int |E_p|^2 dV \int |E_R|^2 dV}{\int |E_p|^2 |E_R|^2 dV} \quad (4.3)$$

where  $E_p$  and  $E_R$  are energy density of pump and Raman mode, respectively.

The threshold power has an inverse square dependence on the quality factor that indicates microcavities with high quality factors require less pump power for stimulated Raman scattering. Total Raman output power is given by [36]

$$P_R = 4 \frac{\omega_R}{\omega_p} \left( 1 + \frac{\tau_{ex}}{\tau_0} \right)^{-2} P_{thresh} \left( \sqrt{\frac{P}{P_{thresh}}} - 1 \right) \quad (4.4)$$

here  $\omega_R$  and  $\omega_p$  are the excitation frequency of Raman and pump modes,  $\tau_0$  and  $\tau_{ex}$  are the intrinsic and external photon lifetimes,  $P$  is the pump power.

## 4.4 Sample Preparation and Experimental Setup

### 4.4.1 Superhydrophobic Coating and Microdroplet Generation

60 mg/ml ethanol dispersion of hydrophobically coated silica nanoparticles (LE1) solution was spin coated on a cover glass. The average contact angle of large water droplets on LE1 surface was measured to be larger than  $150^\circ$ . Water microdroplets with diameters ranging a few up to  $\sim 100 \mu\text{m}$  were generated by an ultrasonic nebulizer onto the prepared superhydrophobic surface.



#### 4.4.2 Humidity Chamber

In order to prevent water microdroplet evaporation, we used a mini humidity chamber. Immediately after microdroplet generation, humidity chamber sealed onto the surface to prevent rapid evaporation of the pure water microdroplets in the absence of pump laser. Figure 4.2 shows the mini humidity chamber that we used to prevent evaporation in our experiments.



**Figure 4.2** Mini humidity chamber

Pump laser causes slight evaporation that is  $<15\%$  change in radius over one minute pumping on individual microdroplets [31]. Diameters of the water microdroplets stated in this chapter correspond to the initial values of the diameter before the application of the pump laser.

### 4.4.3 Optical Setup

The water microdroplets were excited by a frequency-doubled Nd:YAG laser that produces green pulses at the wavelength of 532 nm. The pulse repetition rate and pulsewidth were 1 kHz and 100 ns, respectively. In our experiments, laser pump energies up to 60 mW were available [31]. Pulsed laser was reflected off a dichroic mirror and focused to an estimated 25  $\mu\text{m}$  diameter spot using a microscope objective with 0.80, 60x numerical aperture in inverted geometry. The same microscope objective was used to collect the Raman signal from individual microdroplets.

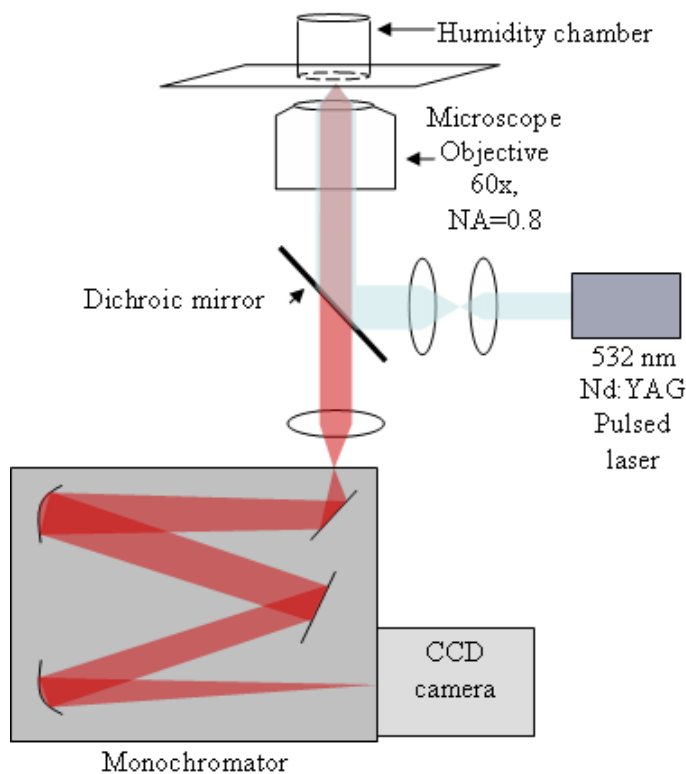


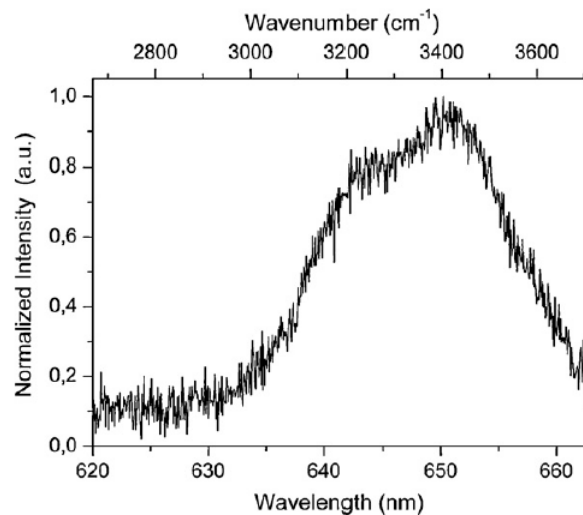
**Figure 4.3** Optical Setup

Raman spectra were recorded with a 0.5-m monochromator and a CCD camera with 0.17 nm spectral resolution [31]. During consecutive acquisitions, the exposure time was followed with 2.2 s readout time. Movies of microdroplets exhibiting Raman lasing were recorded using a band pass filter and a monochrome CCD camera.

## 4.5 Experimental Results

### 4.5.1 Raman Spectrum of Liquid Water

Raman spectra contain information about the molecular structure of the samples, their chemical composition, crystalline properties, and so on [37]. The Raman spectrum of the OH stretching vibrations of liquid water shows the complex nature of this sample. This spectrum varies due to the change in the temperature of the water; its transition into the solid or gas phase [37]. Fluctuations in temperature cause changes in the structure of the water molecules.



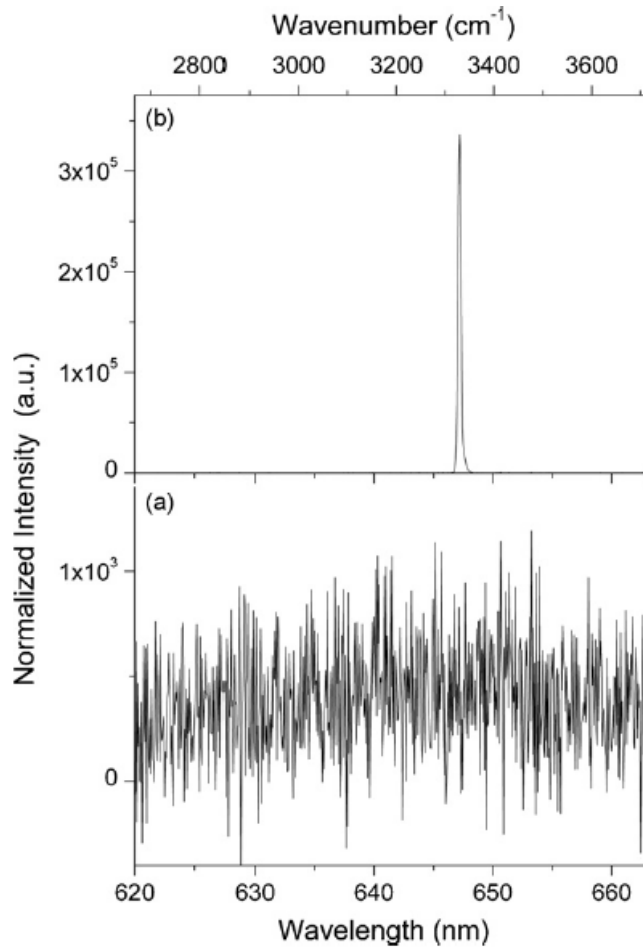
**Figure 4.4** Raman spectrum of liquid water including resonances due to OH-stretching bonds

Figure 4.4 shows the Raman spectrum of the OH-stretching bonds of liquid water located between 2900 and 3700  $\text{cm}^{-1}$  recorded at room temperature. In our experiments, Raman lasing was observed from individual WGMs within this Raman region. Exposure time of the CCD camera was 30 s in the spectrum reported in Figure 4.4.

#### **4.5.2 Raman Lasing from Pure Water Microdroplets**

We observed Raman lasing from individual WGMs routinely during our experiments. Raman lasing occurred within the Raman gain region of pure water near 650 nm where Raman resonances are located. The OH-stretching bonds of water give rise to these Raman resonances [34]. The spectra obtained from a 13  $\mu\text{m}$  diameter water microdroplet exhibiting Raman lasing is shown in Figure 4.5 which was obtained by recording the consecutive WGM intensities of water microdroplet. Intense WGM emission which increases to values more than 25 dB was observed momentarily in Raman gain region at 647 nm providing the clear indication of Raman lasing (Figure 4.5).

We couldn't observe Raman lasing continuously due to thermally induced density fluctuations as observed in previous work of Raman lasing from glycerol-water microdroplets [34]. At moments when water microdroplet was not lasing, the intensity of WGMs dropped down more than 25 dB as shown in consecutive acquisitions in Figure 4.5 [34]. The single peak in the spectrum indicated that it is Raman lasing, shown in Figure 4.5. For the case of cavity enhanced Raman scattering, all the WGMs within the Raman band of water are expected to be present in the spectrum shown in Figure 4.4.



**Figure 4.5** Consecutive spectra recorded from a 13- $\mu\text{m}$  diameter water microdroplet during the (a) “off” and (b) “on” periods of Raman lasing.

We also observed simultaneous lasing at two different WGMs belong to different mode sets as shown in acquisition 10 of Figure 4.6. We did not try to identify the WGMs of Figure 4.5 (b) and Figure 4.6 because of the evaporation during the experiments and the absence of the complete set of WGMs within the Raman gain region, such as those seen in the stimulated Raman scattering spectra [38-40]. We estimated the quality factors of lasing WGMs with the help of peak laser intensity  $\sim 10^8$  W/cm<sup>2</sup> used in our experiments and the Raman gain coefficient of water at 532 nm, which is 0.14 cm/GW. Quality factor that we estimated for WGMs exhibiting Raman lasing is  $\sim 5 \times 10^6$  [41],

which is in agreement with the expected quality factors can be as high as  $\sim 10^8$  for a 10  $\mu\text{m}$  diameter water microdroplet at 532 nm [42].

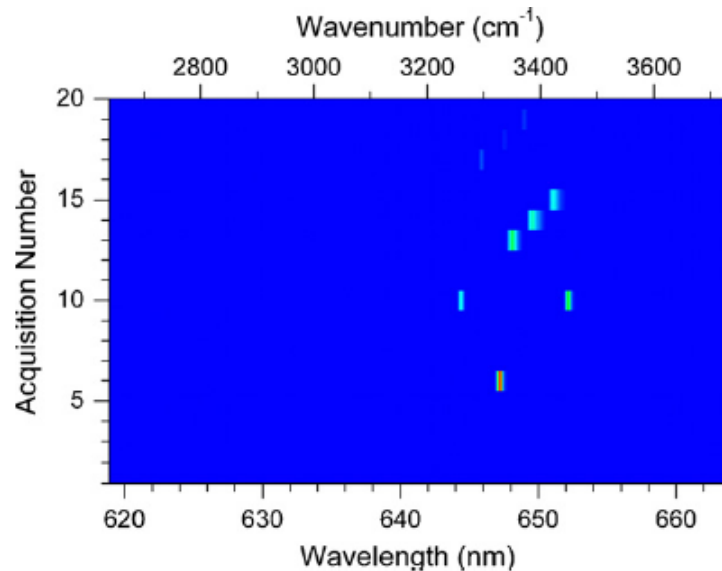


**Figure 4.6** Contour plot of a 13- $\mu\text{m}$  diameter microdroplet exhibiting Raman lasing. Momentary single-mode (acquisitions numbers 6, 13, 14 and 15) and multi-mode (acquisition number 10) Raman lasing is observed.

The time trace of a 14- $\mu\text{m}$  diameter water microdroplet exhibiting Raman lasing is shown in Figure 4.7. This time trace was obtained by analyzing the image sequences of 25 frame/s generated from the microdroplet's Raman signal. The average inter-burst separation was found to be 1.2 s being longer than in the case of glycerol-water microdroplets (0.4 s) using nitrogen purging [34].

Nitrogen purging for pure water experiment was not possible because of the mini humidity chamber that we used in the experiments. Furthermore, it was observed that the longer inter-burst separation caused slower rate of cooling of the microdroplets.

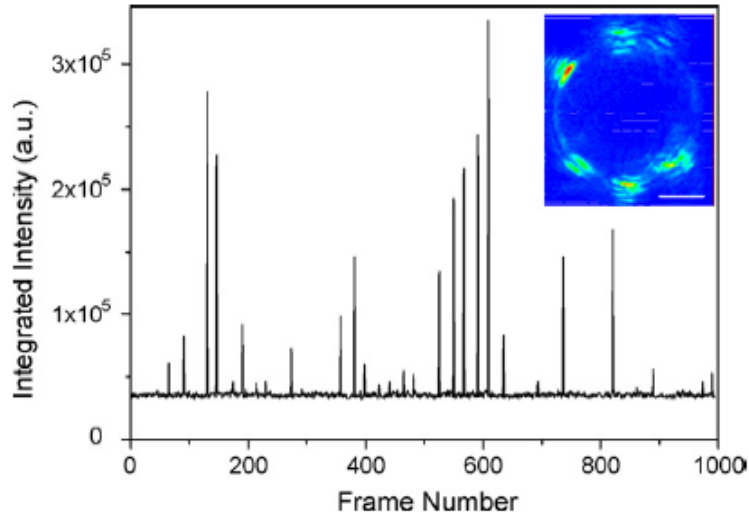


**Figure 4.7** Time trace of the Raman lasing intensity from a 14- $\mu\text{m}$  diameter microdroplet shows the “on/off” behavior. Inset: image used in calculating the time trace.

The time trace shown in Figure 4.7 has a recording rate of 25 frames/s. Average inter-burst separation was observed to be 1.2 s for this microdroplet. Inset shows the image used in calculating the time trace at frame 608, which has the form of a ring. The absence of an emissive plume suggests that aerosol-induced laser breakdown is not observed in our case. This is further supported by the fact that the peak laser intensity used in our experiments ( $\sim 10^8 \text{ W/cm}^2$ ) is approximately ten times smaller than the aerosol-induced laser breakdown threshold (2-3  $\text{GW/cm}^2$ ) for water droplets at 532 nm laser wavelength [43].

## 4.6 Summary

In this chapter, Raman lasing near 650 nm was demonstrated using 13-14  $\mu\text{m}$  diameter water microdroplets pumped with a pulsed, frequency-doubled Nd:YAG laser at 532 nm. In the experiments, stationary, pure water microdroplets were prepared on a superhydrophobic surface. A mini humidity chamber was used, in order to prevent the evaporation of the water microdroplets. Intense laser emission was observed at frequencies corresponding to the whispering gallery mode resonances of the water microdroplets near 650 nm where Raman resonances due to OH-stretching bonds of water are located. The pump laser caused excessive heating that is why the intensity of the lasing WGMs was not sustained during the Raman lasing. The intensity of the lasing WGMs was not sustained during the Raman lasing when excess heat was dissipated due to the pump laser. By the time-dependent intensity traces, the average temporal inter-burst separation was determined. We have observed on-off behavior during Raman lasing; when excess heating was dissipated, Raman lasing was observed to resume. Our results can find applications in the development of novel organic light emitters for short-haul communication systems and in the spectroscopic characterization of water microdroplets on a surface. Furthermore, similar methods may pave the way for the observation of natural lasing in atmospheric aerosols excited by an intense natural pump source such as lightning.



## Chapter 5

### CONCLUSION

In this thesis, we discussed experiments in liquid microdroplets, which serve as optical microcavities. Whispering gallery modes (WGMs) of the liquid microdroplets were the main issue in our experiments because they characterize the optical cavity that we used. By using the natural properties of the liquid microdroplets, we demonstrated nondegeneracy in WGMs of glycerol-water microdroplets and also Raman lasing from stationary pure water microdroplets standing on a superhydrophobic surface. In both of these studies, the superhydrophobic nature of the surfaces helped us to keep the shape of the microdroplets approximately spherical. By this way, we were able to use the whispering gallery modes (WGMs) of the liquid microdroplets for the characterization of optical microcavities.

In the first work, the easily deformable and flexible nature of microdroplets let us observe the non-degenerate cavity modes by the use of a uniform electric field which lifted the azimuthal degeneracy of the WGMs of glycerol-water microdroplets in a controlled manner. As the shape of the microdroplet was changed towards a prolate spheroid due to this uniform electric field, the splitting in the WGMs was observed. At high voltages, resolved nondegenerate cavity modes were shown in this work. The other important result of this study is measurement of the contact angle of microdroplets. Contact angles were estimated by using the difference between measured azimuthal modes and expected modes from an ideal spherical microdroplet. This technique can lead to demonstration of novel electrically tunable devices.

The spherical structure of microdroplets could be well maintained providing the similar mode structure of an ideal spherical resonator by keeping them on superhydrophobic samples. Pure water microdroplets were exposed to a pulsed laser, which allowed us to see Raman lasing. This property can lead us to the realization of tunable microcavity lasers. Our technique can be a good alternative to other solid optical microdroplets standing on a substrate.

## APPENDIX

**\* MATLAB program for simulation of the coupled WGMs.**

**\* This function generates the Spherical Harmonics basis functions of degree L and order M.**

```
% SYNTAX: [Ymn,THETA,PHI,X,Y,Z]=spharm4(L,M,RES,PLOT_FLAG);
% INPUTS:
% L - Spherical harmonic degree, [1x1]
% M - Spherical harmonic order, [1x1]
% RES - Vector of # of points to use [#Theta x #Phi points],[1x2] or [2x1]
% PLOT_FLAG - Binary flag to generates a figure of the spherical harmonic surfaces
% OUTPUTS:
% Ymn - Spherical harmonics coordinates, [RES(1) x RES(2)]
% THETA - Circumferential coordinates, [RES(1) x RES(2)]
% PHI - Latitudinal coordinates, [RES(1) x RES(2)]
% X,Y,Z - Cartesian coordinates of magnitude, squared, spherical harmonic surface
% points, [RES(1) x RES(2)]
% NOTE: It is very important to keep the various usages of THETA and PHI
% straight. For this function THETA is the Azimuthal/Longitude/Circumferential
% coordinate and is defined on the interval [0,2*pi], whereas PHI is the
% Altitude/Latitude/Elevation and is defined on the interval [0,pi]. Also note that
% the conversion to cartesian coordinates requires that PHI be offset by pi/2 so
% that the conversion is on the interval [-pi/2,pi/2].
```

```
function [Ymn,THETA,PHI,Xm,Ym,Zm]=spharm_alper(L,M,RES,PLOT_FLAG);
```

```
% Define constants (REQUIRED THAT L(DEGREE)>=M(ORDER))
if nargin==0
    L=3; % DEGREE
    M=2; % ORDER
    RES=[55 55];
end
if nargin<3
    RES=[25 25];
    PLOT_FLAG=1;
end
```

```
if nargin<4
    PLOT_FLAG=1;
end

if L<M, error('The ORDER (M) must be less than or equal to the DEGREE(L).'); end
THETA=linspace(0,2*pi,RES(1)); % Azimuthal/Longitude/Circumferential
PHI =linspace(0, pi,RES(2)); % Altitude /Latitude /Elevation
[THETA,PHI]=meshgrid(THETA,PHI);

Lmn=legendre(L,cos(PHI));

if L~=0
    Lmn=squeeze(Lmn(M+1,:,:));
end

a1=((2*L+1)/(4*pi));
a2=factorial(L-M)/factorial(L+M);
C=sqrt(a1*a2);

Ymn=C*Lmn.*exp(i*M*THETA);
%Ymn=C*Lmn.*cos(M*THETA);

[Xm,Ym,Zm]=sph2cart(THETA,PHI-pi/2,1);
[Xr,Yr,Zr]=sph2cart(THETA,PHI-pi/2,1);
[Xi,Yi,Zi]=sph2cart(THETA,PHI-pi/2,1);
% [Xp,Yp,Zp]=sph2cart(THETA,PHI-pi/2,angle(Ymn).^2);

if PLOT_FLAG
    surf(Xm,Ym,Zm,abs(Ymn).^2);
    shading flat;
end

return
```

**\* MATLAB program for mode matching**

% Run the peaks\_within\_an\_alpha\_inteval.m routine first. Then enter the  
% wavelengths of the WGMs in the same family in a decreasing wavelength  
% order, then run this program to find best matchig TE or TM modes.

clc;

clear all;

```
%TE_vec=load(sprintf('%s','TE_1_4274.txt'));
%TM_vec=load(sprintf('%s','TM_1_4274.txt'));
%TE_vec=load(sprintf('%s','TE_1_4146.txt'));
%TM_vec=load(sprintf('%s','TM_1_4146.txt'));
%TE_vec=load(sprintf('%s','TE_1_4214.txt'));
%TM_vec=load(sprintf('%s','TM_1_4214.txt'));
TE_vec=load(sprintf('%s','TE_1_4417.txt'));
TM_vec=load(sprintf('%s','TM_1_4417.txt'));
```

```
lambda_vec=[592.81e-9 576.74e-9 561.55e-9];
%lambda_vec=[591.6783e-9 577.6716e-9];
%07 01 09 a01 measured m=16, expected n=48
```

```
%%%
```

```
%lambda_vec=[593.29e-9 577.86e-9 563.27e-9];
%lambda_vec=[597.02e-9 582.54e-9];
%07 01 09 b01 measured m=16, expected n=35
```

```
%lambda_vec=[595.27e-9 578.84e-9 563.35e-9];
%lambda_vec=[602.85e-9 588.90e-9];
%07 01 09 c01 measured m=16, expected n=33,32
```

```
%lambda_vec=[594.13e-9 579.48e-9 565.53e-9];
%lambda_vec=[605.51e-9 589.55e-9];
%07 01 09 d01 measured m=16, expected n=37,36
```

```
%lambda_vec=[594.13e-9 578.95e-9 565.23e-9];
%lambda_vec=[594.68e-9 582.15e-9];
%07 01 09 e01 measured m=16, expected n=36
```

```
%lambda_vec=[590.90e-9 577.37e-9 564.49e-9];
%lambda_vec=[589.33e-9 574.20e-9];
%07 01 09 f01 measured m=16, expected n=39,40
```

```
%%  
%lambda_vec=[590.78e-9 575.42e-9 561.83e-9];  
%lambda_vec=[594.47e-9 577.09e-9];  
%07 01 09 g01 measured m=16, expected n=36  
  
%%  
%lambda_vec=[587.96e-9 573.06e-9 558.94e-9];  
%lambda_vec=[612.38e-9 597.96e-9];  
%07 01 09 h01 measured m=16, expected n=35,36  
  
%%  
%lambda_vec=[593.81e-9 578.73e-9 564.49e-9];  
%lambda_vec=[610.5e-9 595.95e-9];  
%07 01 09 i01 measured m=16, expected n=35,36  
  
%%  
%lambda_vec=[609.14e-9 594.84e-9 581.24e-9];  
%lambda_vec=[605.69e-9 588.25e-9];  
%07 01 09 j01 measured m=16, expected n=38,39  
  
%lambda_vec=[600.05e-9 584.27e-9 569.32e-9];  
%lambda_vec=[611.63e-9 597.45e-9];  
%07 01 09 k01 measured m=16, expected n=34,35  
  
%lambda_vec=[604.78e-9 586.22e-9 568.72e-9];  
%lambda_vec=[596.13e-9 582.59e-9];  
%07 01 09 l01 measured m=16, expected n=29  
  
%%  
%lambda_vec=[612.61e-9 597.12e-9 582.35e-9];  
%lambda_vec=[597.31e-9 582.01e-9];  
%07 01 09 m01 measured m=16, expected n=35,36  
  
%lambda_vec=[610.3e-9 592.69e-9 576.08e-9];  
%lambda_vec=[586.55e-9 570.89e-9];  
%07 01 09 n01 measured m=16, expected n=31  
  
%lambda_vec=[619.21e-9 603.90e-9 589.36e-9];  
%lambda_vec=[586.37e-9 572.78e-9];  
%07 01 09 o01 measured m=16, expected n=36,37  
  
%lambda_vec=[595.02e-9 579.77e-9 565.35e-9];
```

```
%07 01 09 p01 measured m=16, expected n=35
```

```
%lambda_vec=[598.26e-9 583.89e-9 570.18e-9];
%lambda_vec=[616.9147e-9 600.4849e-9];
%07 01 09 r01 measured m=16, expected n=37,38
```

```
%lambda_vec=[592.05e-9 580.58e-9 566.16e-9];
%lambda_vec=[577.5057e-9 561.2532e-9];
%07 01 09 s01 measured m=16, expected n=40,41
```

```
%lambda_vec=[598.15e-9 585.56e-9 573.45e-9];
%lambda_vec=[601.3472e-9 585.7448e-9 570.9107e-9];
%07 01 09 t01 measured m=16, expected n=43
```

```
%lambda_vec=[594.19e-9 581.54e-9 569.43e-9];
%lambda_vec=[623.0187e-9 608.8911e-9 595.5124e-9 582.6743e-9];
%07 01 09 u01 measured m=16, expected n=43
```

```
for ii=1:(length(TE_vec)-length(lambda_vec)+1);
    err_vec(ii)=0;
    for jj=1:length(lambda_vec)
        res_rad(jj)=lambda_vec(jj)*TE_vec(ii+jj-1)/(2*pi);
    end;
    err_vec(ii)=std(res_rad);
%   res_rad=lambda_vec(1)*TE_vec(ii)/(2*pi);
%   for jj=2:length(lambda_vec)
%       alpha_vec(jj)=2*pi*res_rad/lambda_vec(jj);
%       err_vec(ii)=err_vec(ii)+abs(alpha_vec(jj)-TE_vec(ii+jj-1));
%   end;
end
subplot(211)
plot(err_vec,'o')
min_i=find(err_vec==min(err_vec));
min(err_vec)
n_expected=21+min_i
res_rad=610e-9*TE_vec(min_i)/(2*pi)

for ii=1:(length(TM_vec)-length(lambda_vec)+1);
    err_vec(ii)=0;
    for jj=1:length(lambda_vec)
```

---

```
    res_rad(jj)=lambda_vec(jj)*TM_vec(ii+jj-1)/(2*pi);
end;
err_vec(ii)=std(res_rad);
end
subplot(212)
plot(err_vec,'o')
min_i=find(err_vec==min(err_vec));
min(err_vec)
n_expected=22+min_i
res_rad=610e-9*TM_vec(min_i)/(2*pi)
```



**\* Python program for finding all peaks in the spectrum**

```
import scipy
import pylab
from math import *
from scipy.integrate import quad

class fitParameter:
    """Helper class for the function fit"""
    def __init__(self, value):
        self.value = value
    def set(self, value):
        self.value = value
    def __call__(self):
        return self.value

def fit(function, parameters, y, x = None):
    """Fit with formula function"""
    def f(params):
        i = 0
        for p in parameters:
            p.set(params[i])
            i += 1
        return y - function(x)

    if x is None: x = scipy.arange(y.shape[0])
    p = [param() for param in parameters]
    scipy.optimize.leastsq(f, p)

def _findAllPeaks(f, window=(0, 765), search_points=1000):
    """Find all the peaks from the given function f
    and return the X position vectors of positive and negative roots
    as negrootsX, posrootsX."""
    xx=scipy.linspace(window[0], window[1], search_points)
    ydiff=scipy.derivative(f, xx)
    fdiff=scipy.interpolate.interp1d(xx, ydiff)
    frame=scipy.linspace(window[0], window[1], search_points)
    rootlist=[]
    for k in range(len(frame)-1):
        x1=frame[k]
        x2=frame[k+1]
```

```

    v1=fdiff(x1) # function value at point x1
    v2=fdiff(x2) # function value at point x2
    sign = v1 * v2
    if(sign<0): # if they have a different sign
        root=scipy.optimize.brenth(fdiff, x1, x2)
        if(v1 < v2): # negative peak
            print 'negative root found at x='+str(root)
            rootlist.append([root, -1])
        else:
            #print 'positive root found at x='+str(root)
            rootlist.append([root, 1])
    print '%d peaks found in window' % (len(rootlist))
    return scipy.array(rootlist)

def _fitLorentz(sampleX, sampleY, width, x0, y0):
    """Try a fit with the peak separation list listSepa"""

    c=fitParameter(0)
    a=fitParameter(1e8)
    mu=fitParameter(x0)
    b=fitParameter(width)

    def f_lorentz(x):
        result = c() + a() * 1/( (x-mu())**2 + (b()/2)**2)
        return result

    fit(f_lorentz, [c, a, mu, b], sampleY, sampleX)
    #print str([c(), a(), mu(), b()])
    #print ('Fit : center=%.2f (old=%.2f), y0=%.2f, width=%.2f, ' % (mu(), x0, c(),
b()))
    print ('Fit : center=%.2f (old=%.2f), width=%.1f, ' % (mu(), x0, b()) )
    #pylab.plot(sampleX, sampleY, sampleX, f_lorentz(sampleX))
    #pylab.show()
    return mu(), f_lorentz(sampleX)

def _correctPeaks(f, peaksX, peaksWidths):
    peaksY=f(peaksX)
    npeaks=peaksX.size
    print 'number of peaks='+str(npeaks)

```

```

newpeaksX=scipy.zeros_like(peaksX)
newpeaksGamma=scipy.zeros_like(peaksX)
fittedCurves=[]
for k in range(npeaks):
    leftlim=peaksX[k]-peaksWidths[k]/2.5
    rightlim=peaksX[k]+peaksWidths[k]/2.5
    sampleX=scipy.linspace(leftlim, rightlim, 100)
    sampleY=f(sampleX)
    newpeaksX[k], fittedCurveY=_fitLorentz(sampleX, sampleY,
peaksWidths[k], peaksX[k], peaksY[k])
    fittedCurveT=scipy.array([sampleX, fittedCurveY])
    fittedCurve=fittedCurveT.transpose()
    fittedCurves.append(fittedCurve)
return newpeaksX, fittedCurves

```

### \* Fit the peaks

```

import scipy, scipy.optimize
from math import sqrt
import pylab

```

```

def _sepa(peaksX):
    """find the separations between the first peak and the others"""
    npeaks=len(peaksX)
    result=scipy.zeros(npeaks)
    for k in range(npeaks):
        result[k]=peaksX[k]-peaksX[0]
    return result

```

```

def _matchPeaks(h, listSepa):
    """Try a fit with the peak separation list listSepa"""
    N=scipy.size(listSepa) # number of peaks selected
    alist=[]
    for x in range(1, N): # all but the first
        deltaW=listSepa[x]
        a=deltaW / (x**2 + 2*x*h)
        alist.append(a)
    founda=scipy.mean(alist)
    err=scipy.std(alist) / ( sqrt(len(alist)) * founda )
    #err=scipy.std(alist) / ( sqrt(len(alist)) )
    return founda, err

```

---

```

def index(arr, value):
    temparr=abs(arr-value)
    return scipy.argmin(temparr)

# Outputs : m, h, a, err,
#           peaksSepa (for the first plot)
#           foundmlist (for the second plot)
#           founderrcurve (for the errors)
def _findm(peaksX):
    """
    find the best fit for the data
    """
    npeaks=len(peaksX)
    maxh=60
    errorlist=scipy.zeros((npeaks-1, maxh+1, 3))
    alist=scipy.zeros((npeaks-1, maxh+1))
    founderrlist=scipy.zeros((npeaks-1))
    foundalist=scipy.zeros((npeaks-1))
    foundhlist=scipy.zeros((npeaks-1))
    foundmlist=scipy.zeros((npeaks-1))
    founderrlist=scipy.zeros((npeaks-1))
    krange=range(len(peaksX)-1)
    #krange.reverse()
    for k in krange:
        peaksXextr=peaksX[k:]
        peaksSepa=_sepa(peaksXextr)

        for h in range(0, maxh+1):
            errorlist[k, h, 0]=k
            errorlist[k, h, 1]=h
            alist[k, h], errorlist[k, h, 2] = _matchPeaks(h, peaksSepa)

        founderrlist[k]=errorlist[k,:,2].min()

        foundhlist[k]=scipy.argmin(errorlist[k,:,2])
        foundalist[k]=alist[k, foundhlist[k]]
        foundmlist[k]=foundalist[k]+len(peaksSepa)-1

    print 'Computing on %d peaks : a=%0.3f, m in [%d, %d], err=%0.6f \
% (len(peaksSepa), foundalist[k], foundhlist[k], foundmlist[k],
founderrlist[k])

```

```

# at least 10 peaks for the calculation
countlist=scipy.array([sum(foundmlist[:5]==mvalue) for mvalue in foundmlist[:5]])
maxcount=countlist.max()
maxindices=(countlist==maxcount)
print str(foundmlist[maxindices])+' are the most frequent m values'

suberrlist=founderrlist[maxindices]
minerr=min(suberrlist)
bestindex=index(founderrlist, minerr)
#bestindex=(founderrlist==minerr)
foundh=int(foundhlist[bestindex])
foundm=int(foundmlist[bestindex])
founda=float(foundalist[bestindex])
founderr=float(founderrlist[bestindex])
peaksSepa=_sepa(peaksX[bestindex:])
founderrcurve=errorlist[bestindex,:,2]

print 'selected h=%d, m=%d, a=%.3f, err=%.6f' % (foundh, foundm, founda, founderr)
return foundh, foundm, founda, founderr, peaksSepa, foundmlist, founderrcurve

```

### \* Select peaks

```

import scipy

def _selectPeaks(f, rootlist, minPeakAmpl=1000):
    """Select the positive peaks that have an average distance to the surrounding
    negative peaks greater than minPeakAmpl.
    The position of the negative and positive peaks are given by negrootsX,
    posrootsX"""

    npeaks=rootlist[:,0].size
    rootsX=rootlist[:,0]
    rootsY=f(rootsX)

    selPeaks=[]
    # for all the positive roots, find the (up to) two negative roots around it
    for k in range(npeaks):
        if(rootlist[k,1]>0): # consider only positive peaks
            amplitudes=[]

```

```

    radii=[]
    if(k!=0):
        amplitudes.append(abs(rootsY[k-1]-rootsY[k]))
        radii.append(abs(rootsX[k-1]-rootsX[k]))
    if(k!=(npeaks-1)):
        amplitudes.append(abs(rootsY[k+1]-rootsY[k]))
        radii.append(abs(rootsX[k+1]-rootsX[k]))
    amplitude=scipy.array(amplitudes).min()
    width=2*scipy.array(radii).mean()
    if(amplitude > minPeakAmpl): # validate this peak
        selPeaks.append([rootlist[k,0], width])
        print ('Selected peak at x=%.2f with width=%.2f' %
(rootlist[k,0], width))

    output=scipy.array(selPeaks)
    print '%d peaks selected out of %d' % (len(selPeaks), npeaks)
    return output

```

### \* Smooth function

```
import scipy
```

```
def _smooth(x>window_len=10>window='hanning'):
    """smooth the data using a window with requested size.
```

This method is based on the convolution of a scaled window with the signal. The signal is prepared by introducing reflected copies of the signal (with the window size) in both ends so that transient parts are minimized in the beginning and end part of the output signal.

input:

x: the input signal  
 window\_len: the dimension of the smoothing window  
 window: the type of window from 'flat', 'hanning', 'hamming', 'bartlett', 'blackman'  
 flat window will produce a moving average smoothing.

output:

the smoothed signal

example:

```
t=linspace(-2,2,0.1)
```

```
x=sin(t)+randn(len(t))*0.1
y=smooth(x)
```

see also:

```
numpy.hanning, numpy.hamming, numpy.bartlett, numpy.blackman, numpy.convolve
scipy.signal.lfilter
```

TODO: the window parameter could be the window itself if an array instead of a string  
""

```
if x.ndim != 1:
    raise ValueError, "smooth only accepts 1 dimension arrays."
```

```
if x.size < window_len:
    raise ValueError, "Input vector needs to be bigger than window size."
```

```
if window_len<3:
    return x
```

```
if not window in ['flat', 'hanning', 'hamming', 'bartlett', 'blackman']:
    raise ValueError, "Window is one of 'flat', 'hanning', 'hamming', 'bartlett',
'blackman'"
```

```
s=scipy.r_[2*x[0]-x[window_len:1:-1],x,2*x[-1]-x[-1:-window_len:-1]]
#print(len(s))
```

```
if window == 'flat': #moving average
    w=scipy.ones(window_len,'d')
```

```
else:
    w=eval('scipy.'+window+'(window_len)')
```

```
y=scipy.convolve(w/w.sum(),s,mode='same')
return y[window_len-1:-window_len+1]
```

**BIBLIOGRAPHY**

- [1] H. Yokohama, "Physics and device applications of optical microcavities," *Science* **256**, 66 (1992)
- [2] V.S. Ilchenko and A.B. Matsko, "Optical resonators with whispering gallery modes-Part 2: Applications," *IEEE Journal of Selected Topics in Quantum Electronics*, vol. 12, pp. 15 (2006)
- [3] C. J. Hood, H. J. Kimble, and J. Ye, "Characterization of high-finesse mirrors: Loss, phase shifts, and mode structure in an optical cavity" *Phys. Rev. A*, vol. 57, pp. 2293-2296, 2001.
- [4] T. Baba, P. Fujita, A. Sakai, M. Kihara, and R. Watanabe, "Lasing characteristics of GaInAsP-InP strained quantum-well microdisk injection lasers with diameter of 2-10  $\mu\text{m}$ ," *IEEE Photon. Tech. Lett.*, vol. 9, pp. 878-880, 1997.
- [5] A. Belarouci, K. B. Hill, Y. Liu, Y. Xiong, T. Chang, and A. E. Craig, "Design and modeling of waveguide-coupled microring resonator," *Journal of Luminescence*, vol. 94-95, pp. 35-38, 2001.
- [6] V. L. Seguin, "Whispering-gallery mode lasers with doped silica microspheres," *Optical Materials*, vol. 11, pp. 153-165, 1999.
- [7] J. Scheuer and A. Yariv, "Annular Bragg Defect mode Resonators," *J. Opt. Soc. Am. B*, vol. 20, pp. 2285-2291, 2003.



- 
- [8] D. K. Armani, T. J. Kippenberg, S. M. Spillane, and K. J. Vahala, "Ultra-high-Q toroid microcavity on a chip," *Nature*, vol. 421, pp. 925-928, 2003.
- [9] G. S. Solomon, M. Pelton, and Y. Yamamoto, "Single-mode Spontaneous Emission from a Single Quantum Dot in a Three-Dimensional Microcavity," *Phys. Rev. Lett.*, vol. 86, pp. 3903-3906, 2001.
- [10] O. Painter, R. K. Lee, A. Scherer, A. Yariv, J. D. O'Brien, P. D. Dapkus, and I. Kim, "Two-dimensional photonic band-gap defect mode laser," *Science*, vol. 284, pp. 1819, 1999.
- [11] A. Kiraz, A. Kurt, M. A. Dündar, and A. L. Demirel, "Simple largely tunable optical microcavity," *Appl. Phys. Lett.*, vol. 89, pp. 081118, (2006)
- [12] K. J. Vahala, "Optical microcavities," *Nature*, vol. 424, pp. 839-846, 2003
- [13] H. Walther, B.T.H. Varcoe, B.G. Englert and T. Becker, "Cavity quantum electrodynamics," *Rep. Prog. Phys.* **69**, 1325-1382 (2006)
- [14] V.S. Ilchenko, X. S. Yao, L. Maleki, "Ultra-high Q whispering gallery microcavities for narrow-linewidth lasers and optoelectronic oscillators,"
- [15] Andrea M. Armani, "Microcavity gas and vapor sensors and detection methods," US patent, USPC Class: 356437
- [16] S. Kuiper and B. H. W. Hendricks, "Variable-focus liquid lens for miniature cameras," *Appl. Phys. Lett.* **85**, 1128-1130 2004.

- 
- [17] A. Ashkin and J. M. Dziedzic, "Optical Levitation of Liquid Drops by Radiation Pressure," *Science* **187**, 1073 (1975).
- [18] A. Ashkin and J. M. Dziedzic, "Observation of Resonances in the Radiation Pressure on Dielectric Spheres," *Phys. Rev. Lett.* **38**, 1351 (1977).
- [19] A. Kiraz, A. Kurt, M. A. Dündar, M. Y. Yüce, and A. L. Demirel, "Volume stabilization of single, dye-doped water microdroplets with femtoliter resolution," *J. Opt. Soc. Am. B* **24**, 1824-1828 (2007).
- [20] A. Kiraz, A. Sennaroglu, S. Doğanay, M. A. Dündar, A. Kurt, H. Kalaycioglu, and A. L. Demirel, "Lasing from single, stationary, dye-doped glycerol/water microdroplets located on a superhydrophobic surface," *Opt. Commun.* **276**, 145-148 (2007).
- [21] M.H. Fields, J. Popp, R. K. Chang, "Nonlinear Optics in Microspheres,"
- [22] J.P. Barton, D.R. Alexander and S.A. Schaub, "Internal and near-surface electromagnetic fields for a spherical particle irradiated by a focused laser beam," *J. Appl. Phys.*, vol. 64, pp. 1632-1639, 1988
- [23] V.S. Ilchenko and A.B. Matsko, "Optical resonators with whispering-gallery modes- Part 2: Applications," *IEEE J. Sel. Top. Quantum Electron.* **12**, 15-32 (2006).
- [24] M.I. Mishchenko, A.A. Lacis, "Morphology-dependent resonances of nearly spherical particles in random orientation," *Appl. Opt.*, **42**, 5551-5556 (2003)

- 
- [25] S.C. Yorulmaz, M. Mestre, M. Muradoglu, B.E. Alaca, A. Kiraz, "Controlled observation of nondegenerate cavity modes in a microdroplet on a superhydrophobic surface," *Opt. Commun.* **282**, 3024-3027 (2009)
- [26] N. Bentesis and S. Krause, "Droplet deformation in Dc electric fields: The extended leaky dielectric model," *Langmuir*, **21**, 6194-6209 (2005)
- [27] G. Chen, M.M. Mazumder, Y.R. Chemla, A. Serpenguzel, and R.K. Chang, "Wavelength variation of laser emission along the entire rim of slightly deformed microdroplets," *Optics Letters*, Vol. 18, No.23 (1993)
- [28] A. Kiraz, Y. Karadag, A. F. Coskun, "Spectral tuning of liquid microdroplets standing on a superhydrophobic surface using electrowetting," *Appl. Phys. Lett.* **92** (2008) 191104
- [29] M.Y. Yuce, A.L.Demirel, F.Menzel, "Tuning the Surface Hydrophobicity of Polymer/Nanoparticle Composite Films in the Wenzel Regime by Composition," *Langmuir* **21** (2005) 5073
- [30] A. Kiraz, Y. Karadag, S.C. Yorulmaz, M. Muradoglu, "Reversible photothermal tuning of a salty water microdroplet," *Phys. Chem. Chem. Phys.* **11** 275 (2009) 2597
- [31] A. Kiraz, S. C. Yorulmaz, M. Yorulmaz, and A. Sennaroglu, "Raman lasing near 650 nm from pure water microdroplets on a superhydrophobic surface," *Photon. Nanostruct.: Fundam. Appl.* (2009)
- [32] M.M. Dumitrescu, M.J. Saarinen, M.D. Guina, and M.V. Pessa,

- “High-speed resonant cavity light-emitting diodes,” *IEEE J. Sel. Topics Quantum Electron.*, vol. 8, no.2, pp. 219-230, Mar. /Apr. 2002.
- [33] S.M. Spillane, T.J. Kippenberg, and K.J. Vahala,  
“Ultralow-threshold Raman laser using a spherical dielectric microcavity,”  
*Nature*, vol. 415, no. 6872, pp. 621-623, 2002
- [34] A. Sennaroglu, A. Kiraz, M.A. Dunder, A. Kurt, and A.L. Demirel,  
“Raman lasing near 630 nm from stationary glycerol-water microdroplets on a superhydrophobic surface,” *Optics Letters*, vol. 32, pp. 2197-2199, 2007
- [35] C.V. Raman, F.R.S., “A new radiation,” *Indian Journal of Physics*, 2 (1928) 387
- [36] Kerry Vahala, “Optical Microcavities,” World Scientific, 2004
- [37] *Optics and Spectroscopy*, Vol. 96, No. 4, 2004, pp. 512–514.
- [38] J.B. Snow, S.X. Qian, R.K. Chang, “Stimulated Raman scattering from individual water and ethanol droplets at morphology-dependent resonances,” *Opt. Lett.* 10 (1) (1985)
- [39] R.G. Pinnick, A. Biswas, P. Chylek, et.al. *Opt. Lett.* 13 (1988) 494
- [40] J.G. Xie, T.E. Ruekgauer, J. Gu, et.al. *Appl. Opt.* 33 (3) (1994) 368
- [41] M.M. Tilleman, R. Grasso, *Appl. Phys. B* 61 (1995) 581
- [42] A. Serpenguzel, J.C. Swindal, R.K. Chang, et.al. *Appl. Opt.* 31 (18) (1992) 3543

- [43] R. G. Pinnick, P. Chylek, M. Jarzembski, et.al. *Appl. Opt.* 27 (7) (1988) 987.